Journal of Sound and Vibration 532 (2022) 116989

Contents lists available at ScienceDirect

Journal of Sound and Vibration

journal homepage: www.elsevier.com/locate/jsvi

Experimental investigations of indirect noise due to modulation of axial vorticity and entropy upstream of a choked nozzle

L. Hirschberg [a,1], F. Bake [b,2], K. Knobloch [c,3], S.J. Hulshoff [d,4], A. Hirschberg [e,*,5]

[a] Department of Mechanical Engineering, Imperial College London, 58 Princes Gate, London SW7 1AY, UK
[b] Division for Acoustic and Electromagnetic Methods, Department of Non-destructive Testing, Bundesanstalt für Materialforschung und -prüfung (BAM), Unter den Eichen 87, 12205 Berlin, Germany
[c] Institute of Propulsion Technology, Engine Acoustics, German Aerospace Center (DLR), Mueller-Breslau-Str. 8, 10623 Berlin, Germany
[d] Faculty of Aerospace Engineering, Delft University of Technology, Kluyverweg 1, 2629HS Delft, The Netherlands
[e] Department of Applied Physics, Fluids and Flows, Eindhoven University of Technology, P.O. Box 513, 5600 MB Eindhoven, The Netherlands

ARTICLE INFO

Keywords:
Aeroacoustics
Indirect combustion noise
Vorticity noise
Entropy noise
Swirl

ABSTRACT

An experimental cold-gas study of the response of a choked convergent–divergent nozzle to swirl perturbations is presented. The perturbations were obtained by means of upstream unsteady tangential injections into initially steady flows with different values of steady background swirl. The swirl perturbations induced changes in the axial mass-flow rate, due to either their ingestion or evacuation by the nozzle. This in turn caused a downstream acoustic response. For low-intensity background swirl the responses were found to be similar to those obtained without steady background swirl. Perturbations of a high-intensity background swirl led to different effects. For long injection times, the negative mass-flow rate modulation occurred in two stages. The first stage was similar to that of the background-swirl free case. The second stage occurred after a short time delay, and induced a much stronger negative acoustic response. This unexpected behavior suggests that a significant part of the tangentially injected fluid flows upstream inducing an accumulation of swirl, which is – after tangential injection is ceased – suddenly cleared out through the nozzle. A scaling rule for the amplitudes of these acoustic responses is reported. Furthermore, quasi-steady models, based on steady-state measurements are proposed. These models predict the downstream acoustic response amplitude within a factor two. Additionally, preliminary empirical evidence of the effect of swirl on the downstream acoustic response due to the interaction of entropy patches with a choked nozzle is reported. This was obtained by comparison of sound produced by abrupt radial or tangential sonic injection, upstream from the choked nozzle, of air from a reservoir at room temperature to that from a reservoir with a higher stagnation temperature. Because the mass flow through the nozzle does not increase instantaneously, the injected higher-enthalpy air accumulates upstream of the injection-port position in the main flow. This eventually induces a large downstream acoustic pulse when tangential injection is interrupted. The magnitude of the resulting sound pulse can reach that of a quasi-steady response of the nozzle to a large air patch with a uniform stagnation temperature equal to that of the upstream-injected heated air. This hypothesis is

* Corresponding author.
E-mail address: a.hirschberg@tue.nl (A. Hirschberg).
[1] Research associate at Imperial College London.
[2] Head of the Division for Acoustic and Electromagnetic Methods, Bundesanstalt für Materialforschung und -prüfung (BAM).
[3] Damping and Core Noise Team leader at the German Aerospace Center.
[4] Assistant Professor at Delft University of Technology.
[5] Professor emeritus of Eindhoven University of Technology.

https://doi.org/10.1016/j.jsv.2022.116989
Received 13 November 2021; Received in revised form 19 April 2022; Accepted 26 April 2022
Available online 6 May 2022
0022-460X/© 2022 The Author(s). Published by Elsevier Ltd. This is an open access article under the CC BY license (http://creativecommons.org/licenses/by/4.0/).

consistent with the fact that the initial indirect-sound pulse is identical to one obtained with unheated air injection. The authors posit that – given all of the insight gleaned from them in this case – acoustic measurements of indirect sound appear to be a potentially useful diagnostic tool.

1. Introduction

Engineering systems employing turbulent combustion usually have high levels of noise production, due both to direct and indirect combustion-noise sources. Direct sources, due to unsteady gas expansion in flames, have been widely studied [1–3]. Indirect sources include entropy noise and vorticity noise. In particular, both entropy patches and vortices produce sound waves as they exit the combustion chamber through a nozzle or turbine. Some of these sound waves are radiated into the environment, and some are reflected back into the combustion chamber. The latter can produce new entropy patches and vortices, which in turn produce new sound waves as they exit the combustion chamber. Under unfavorable circumstances, this results in a feedback loop which promotes combustion instability or self-sustained pressure pulsations. Thermoacoustic combustion-chamber instabilities driven by indirect-combustion noise are a potential issue in aeroengines and electrical-power generation turbines [2,3]; and self-sustained pressure pulsations are a well-known problem in large solid rocket motors [4–9].

In order to cultivate fundamental understanding of complex phenomena such as indirect-combustion noise, it is standard practice to design experiments in which only one effect is dominant [6,10–16]. A good example of this are the cold-gas – viz. without combustion – scale experiments of self-sustained pressure pulsations in solid rocket motors reported by Anthoine et al. [6]. Indeed, these demonstrated the importance of the integrated nozzle's nozzle-cavity volume on indirect noise produced by essentially nonlinear azimuthal–vortex–nozzle interaction. Another example is Bake's et al. [10] canonical entropy-noise experiment. Moreover, the practice of studying indirect-noise sources in isolation has also been successfully used for the development of analytical and numerical indirect-combustion noise models [17–19].

Of the two indirect-combustion noise sources, entropy noise has been the most widely studied, as evidenced by the high number of citations of two seminal articles by Marble & Candel [17] and Ffowcs Williams & Howe [18]. Vorticity noise, in contrast, has received far less attention.

Kings and Bake [11,12] performed a series of unique experiments with the aim of advancing the fundamental understating of vorticity noise using a so-called "*Vorticity Wave Generator*". In their experiment a strong swirl was introduced upstream from a choked convergent–divergent nozzle by means of unsteady tangentially injection. This swirl convected downstream where it interacted with the choked nozzle producing an acoustic response recorded in the microphone section downstream from the nozzle. Besides performing acoustic measurements, Kings [12] made extensive hot-wire measurements of the upstream flow for a fixed tangential injection condition. These measurements provide evidence of the swirling nature of the upstream-generated structure created by means of unsteady tangential injection. Moreover, they show that the swirl changes over time — starting as a thin wall-bounded jet and evolving to a solid-body like rotation around $t = 29$ ms after the trigger for the start of tangential injection.

Kings and Bake [11] hypothesized that the sound production in their experiments was due to the "*acceleration of artificial vorticity waves*" through the nozzle. However, subsequent analysis of Kings and Bake's data by Hirschberg et al. [20,21] and fresh experiments with an improved experimental setup [13,16] showed that in Kings and Bake's [11,12] experiment the sound production mechanism is the change in axial mass-flow rate as the upstream generated swirl structure is ingested or evacuated by the nozzle [13,16,21].

Note that the most arresting effect of axially-oriented vorticity–nozzle interaction is observed for tangential injection (in the azimuthal direction). When radial injection is used there is no net swirl. However, axially-oriented vorticity generated by radial injection can also result into sound generation by interaction with the nozzle [22].

Furthermore, Hirschberg et al. [20] showed that entropy noise and normal shock contributions to the downstream recorded acoustic response are negligible. This led Hirschberg et al. [13,16] to note that: when it comes to vorticity noise, one should distinguish between sound produced by vorticity oriented normal to the main flow (e.g. the azimuthal–vortex–nozzle interaction in the experiment of Anthoine et al. [6]), and that produced by vorticity oriented parallel to the main flow (axial vorticity) [13,21]. The latter is expected to be an issue in hybrid-rocket engines [23,24], gas turbines, and aeroengines, in which combustion is normally swirl stabilized. In these systems, a significant permanent axial vorticity component is present, the perturbations of which are a potential source of sound when interacting with the combustion chamber exit. Howe and Liu [25] considered the sound generated by a small perturbation of a permanent subsonic swirling flow passing through a contraction in a pipe. In the present paper, the sound generation by large swirl perturbations passing through a choked nozzle is studied experimentally.

The setup used by Kings and Bake [11] had two major shortcomings [13,21]:

1. The acoustic signal recorded downstream from the nozzle was obscured by acoustic reflections at the downstream open-pipe termination.
2. The tangentially-injected mass-flow rate was undetermined.

Ergo, Hirschberg et al. [16] made the following improvements to the experimental setup:

1. The elongation of the downstream pipe section to allow the measurement of an anechoic signal of ca. 140 ms. This made the measurement of the acoustic response due to swirl–nozzle or entropy–swirl–nozzle interaction possible.
2. The addition of an unsteady injection reservoir of known volume, $V_{\text{inj}} = 2.8 \times 10^{-3}$ m^3. Through a calibration procedure – described in Refs. [13,16] – the injection-reservoir pressure p_{inj} was then related to the unsteady upstream-injected mass-flow rate $\dot{m}_{\text{inj}}$.

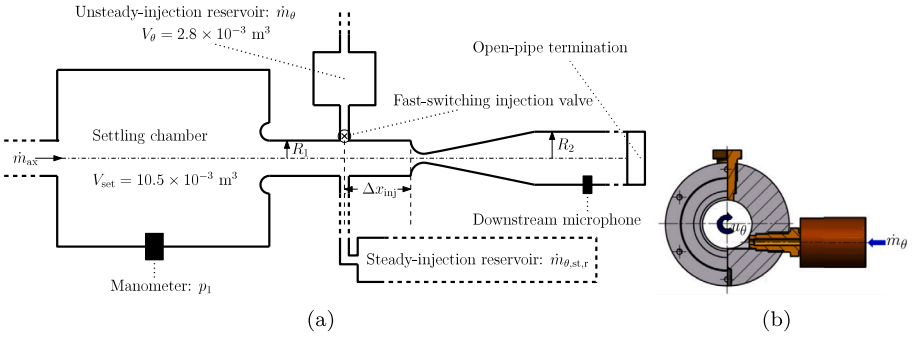

Fig. 1. (a) Sketch of the acoustic measurement setup for the swirl–nozzle interaction experiments. (b) Unsteady tangential-injection system.

Hirschberg et al. [16] used the improved experimental setup to perform fresh experiments. The downstream acoustic response due to swirl–nozzle interaction was found to scale with the square of the unsteady-injected tangential mass-flow rate. Hirschberg et al. [16] found that the ingestion and evacuation of the swirl by the choked nozzle produced different amplitudes of the downstream acoustic response. This is attributed to the difference in the swirl at the start (wall-bounded jet) and end (solid-body rotation) of the injection event. Hirschberg et al. [16] developed an empirical quasi-steady model from steady-flow measurements. Their quasi-steady model provided good predictions for the amplitude of the downstream acoustic signal due to the evacuation of swirl. In contrast, it only provided an order-of-magnitude prediction for the amplitude due to swirl ingestion. However, Hirschberg's et al. [16] experiments and analysis showed that – at least in first-order approximation – the acoustic response amplitude can be described by a quasi-steady model [16]; and that the acceleration of vorticity does not play a leading-order role in its determination. Please note that the quadratic response to the swirl magnitude implies that a linear theory will not predict any indirect noise production due to a small swirl perturbation in the absence of a permanent swirl.

In rocket motors, upstream-generated background swirl can be applied to modulate the axial mass-flow rate and thrust [26]. Baston and Sforzini [27] point out that the increase in chamber pressure due to swirl in the nozzle throat leads to a higher burning rate of the propellant in solid rocket motors. They also state [27]: "*The action of swirling flow on the burning surface of the propellant can cause grain erosion aggravating the situation. These events coupled with the effect of centrifugal force on the combustion mechanism of the propellant may cause the chamber pressure to exceed the structural limits of the motor case, ending in catastrophic failure*". Recent numerical simulation investigations by Sharma and Majdalani [24] of the effect of the exit nozzle geometry on steady flow in a swirl chamber, indicate that complex bidirectional flow can occur. Sharma and Majdalani [24] also provide a review of studies of steady flow in swirl chambers.

We note that whereas the effect of a permanent swirl on the axial mass-flow rate and thrust of rocket engines has been extensively studied [26–29], the dynamical response of such systems has – to date – not systematically been investigated experimentally. In this paper, hitherto unreported results and analysis of an experimental investigation of the dynamic response of a choked nozzle due to the perturbation of a steady background swirl are presented. An improved empirical quasi-steady model for the analysis of these experiments is proposed. In these experiments, the tangentially-injected gas has the same reservoir temperature as the steady-background flow. Here these experiments will be referred to as swirl–nozzle interaction experiments.

In a complementary set of preliminary experiments, the effect of upstream injection with a higher reservoir temperature is explored. This involves a combination of swirl–nozzle and entropy–nozzle interaction. Here, these complementary experiments are referred to as entropy–swirl–nozzle interaction experiments.

In §2 a description of the experimental setups and signal processing is provided. This section is divided into §2.1 and §2.2 for the swirl–nozzle interaction experiments and entropy–swirl–nozzle interaction experiments, respectively. Results and analysis of the swirl–nozzle interaction experiments and entropy–swirl–nozzle interaction experiments are presented in §3 and §4. Conclusions are drawn in §5. In Appendix A a derivation for the calculation of the azimuthal velocity at the nozzle inlet based on the measurement of the static pressure at the nozzle throat is provided. A quasi-steady theory for the acoustical reflection coefficient at the nozzle inlet is provided in Appendix B. An estimation of the direct sound due to transmission of reservoir pressure fluctuations through the nozzle is provided in Appendix C.

2. Description of experimental setups and signal processing

2.1. Swirl–nozzle interaction experiments

2.1.1. Acoustic measurements setup

The presently-reported acoustic-measurement results were obtained with a cold-gas experimental model designed to study unsteady swirl–nozzle interaction in isolation; viz., in the absence of combustion. In Fig. 1(a), a sketch of the experimental setup is shown. The authors note that the setup is a variant of the one used by Hirschberg et al. [13,16] for their background-swirl free swirl–nozzle interaction experiments. Indeed, the modification consisted of adding an injection port (convergent nozzle) of radius

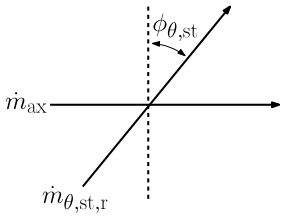

Fig. 2. Definition of the steady tangential-injection angle $\phi_{\theta,\mathrm{st}}$.

$R_{\theta,\mathrm{st}} = 1.25$ mm at a distance $\Delta x_{\mathrm{inj}} = 85$ mm from the convergent–divergent nozzle inlet. Through this port a steady tangential mass-flow rate, $\dot{m}_{\theta,\mathrm{st,r}}$, was injected at an angle of $\phi_{\theta,\mathrm{st}} = 10°$ (defined with respect to the normal on main flow direction as sketched in Fig. 2). This steady tangential mass-flow rate was established by means of an upstream Bronkhorst F-203AV linear resistance flow controller.

In Fig. 1(b), a sketch of the unsteady tangential-injection system is shown. The unsteady injection port was at the same distance $\Delta x_{\mathrm{inj}} = 85$ mm from the convergent–divergent nozzle inlet as the steady tangential-injection port. It was placed diametrically opposite to the steady-injection port and has the same port radius ($R_\theta = 1.25$ mm). The design details of the fast-switching injection valve used for impulsive-tangential injection can be found in Ref. [30]. The opening and closing of the valve, i.e. an injection event, was triggered with a rectangular-electrical pulse with a pulse width τ_{valve}.

The rectangular-trigger signals used to open and close the fast-switching valve, τ_{valve}, were user set. One should note that in practice the actual impulsive-injection time, τ_{imp}, is longer than τ_{valve}. How much longer τ_{imp} is — depends on the injection-reservoir pressure. It ranges between a few milliseconds longer for the lowest injection reservoir pressure to ca. 14 ms for the highest injection reservoir pressure. In Ref. [13], it is explained how one can determine τ_{imp} from the upstream-measured acoustic response p_1'.

The injection valve was connected to a $V_\theta = 2.8\times10^{-3}$ m^3 tangential-injection reservoir with a pressure p_θ by means of a 150 mm long hose with an inner diameter of 10 mm. Static calibration by means of a Bronkhorst F-203AV linear resistance flow meter as detailed in Refs. [13,16], was used to determine the relationship between the unsteady-injection reservoir pressure p_θ and the injected unsteady mass-flow rate $\dot{m}_\theta$. For a choked unsteady-injection port, one has [13,16] for a reservoir at room temperature ($T_\theta = 293.9K$):

$$\dot{m}_\theta = \alpha_{\mathrm{crt}} p_\theta \tag{1}$$

where $\alpha_{\mathrm{crt}} = 6.676\times10^{-9}$ kg s^{-1} Pa^{-1}. Assuming an ideal gas with constant specific heat ratio γ, one has:

$$\dot{m}_\theta = \frac{\gamma p_\theta}{c_\theta}\pi(R^*)^2\left(\frac{2}{\gamma+1}\right)^{\frac{\gamma+1}{2(\gamma-1)}} \tag{2}$$

Hence, for $\gamma = 1.4$, one has $R^* = 0.948$ mm. Note that for the entropy–swirl–nozzle interaction experiments (Sections 2.2 and 4), injection was done at higher T_θ. For these entropy–swirl–nozzle interaction experiments, this relation will be used to calculate the injected mass flow $\dot{m}_\theta$.

The pipe section of radius, $R_1 = 15$ mm upstream from the convergent–divergent nozzle had a length L_1. Most of the experiments reported here are for $L_1 = 220$ mm. A few additional experiments were carried out with $L_1 = 340$ mm. Upstream from its bell-mouth inlet was a settling chamber with volume, $V_{\mathrm{set}} = 10.5\times10^{-3}$ m^3. A Bronkhorst F-203AV linear resistance flow controller upstream from the settling chamber inlet was used to set an axial mass-flow rate $\dot{m}_{\mathrm{ax}}$. The contraction ratio of the nozzle was $R_1^2/R_{\mathrm{th}}^2 = 16$, with the throat radius $R_{\mathrm{th}} = 3.75$ mm. The wall of the upstream pipe and the convergent–divergent nozzle inlet formed a right angle. The nozzle's divergent section was 250 mm long, and led to a 25 m downstream section of radius $R_2 = 20$ mm. At a distance 1150 mm downstream from the nozzle throat, a GRAS 40BP 1/4" ext. polarized pressure microphone was mounted flush in its walls, calibrated using a Brüel & Kjaer model 4228 pistonphone at $|p_{\mathrm{ref}}'| = 123.92$ dB and $f_{\mathrm{ref}} = 251.2$ Hz. This 25 m downstream section made reflection-free recording of vorticity noise possible for ca. 140 ms after the downstream-traveling acoustic wave generated by swirl–nozzle interaction passed the microphone.

As in Ref. [13], the signal p_2' was phase averaged over 100 successive experiments. These were performed with a 3 s interval between two successive injection events. Details about this phase-averaging technique can be found in Refs. [11,12]. To facilitate the interpretation of the data, a low-pass filter with cut-off frequency $f_c = 234$ Hz was also applied [13]. The latter was used to remove the strong quarter-wavelength oscillations of the upstream pipe at $f_1 = c_1/(4L_1)$.

At the beginning of each measurements series the atmospheric pressure p_{atm} was measured by means of a Wuntronic GmbH temperature/airhumidity/atmospheric pressure transmitter Model T7510. The relative pressure in the settling chamber, $p_1 - p_{\mathrm{atm}}$ was determined by means of a MKS Baratron 220D-26159 (1000 mBar) manometer. The temperature in the lab was also measured, and found to be $T_{\mathrm{atm}} = 293.9$ K. It was assumed that $T_1 = T_{\mathrm{atm}}$.

2.1.2. Steady-measurements setup

In §3, a sketch of the setup used to perform steady-state flow measurements is shown. The setup was used to establish a steady-swirl component on a steady axial flow. This was the same setup as for the unsteady-injection experiment described above

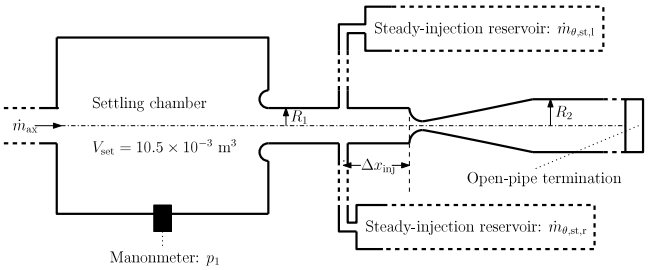

Fig. 3. Steady-state measurement setup for the swirl–nozzle interaction experiments.

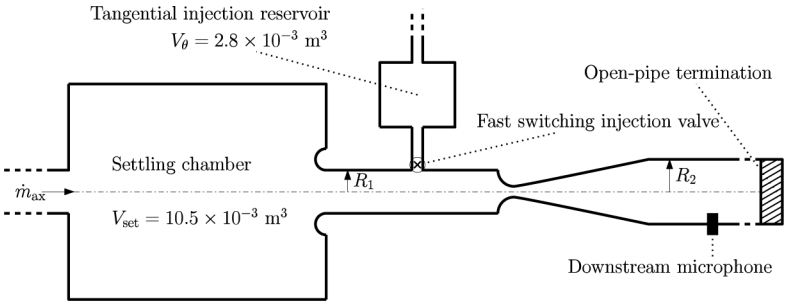

Fig. 4. Sketch of the entropy–swirl–nozzle interaction experimental setup.

(§2.1.1), except that two Bronckhorst F-203AV linear resistance flow controllers were used to set the tangential-injection flow rates through the injection ports. The mass-flow rates established through the right-hand and left-hand port will be referred to as $\dot{m}_{\theta,\mathrm{st,r}}$ and $\dot{m}_{\theta,\mathrm{st,l}}$, respectively. In all experiments the total mass-flow rate was kept constant at 1.194×10^{-2} kg s^{-1}; viz., $\dot{m}_{\mathrm{tot}} = \dot{m}_{\theta,\mathrm{st,r}} + \dot{m}_{\theta,\mathrm{st,l}} + \dot{m}_{\mathrm{ax}} = 1.194 \times 10^{-2}$ kg s^{-1}. I.e., whenever e.g. $\dot{m}_{\theta,\mathrm{st,r}}$ was varied, $\dot{m}_{\mathrm{ax}}$ and $\dot{m}_{\theta,\mathrm{st,l}}$ were varied such that $\dot{m}_{\mathrm{tot}}$ remained 1.194×10^{-2} kg s^{-1}.

To ensure that a steady state was reached, every time the combination of mass-flow rates was varied, a period of five minutes was allowed to elapse before pressure measurements were carried out. The relative pressure in the settling chamber, $p_1 - p_{\mathrm{atm}}$, was measured by means of a MKS Baratron 220D-26159 (1000 mBar) manometer. The atmospheric pressure p_{atm} was determined by means of a Wuntronic GmbH temperature/air-humidity/atmospheric pressure transmitter Model T7510. The static wall pressure p_{th} at the throat of the nozzle was also measured by means of the MKS Baratron 220D-26159 (1000 mBar) manometer.

2.2. Entropy–swirl–nozzle interaction experiments

The setup for the entropy–swirl–nozzle interaction experiments employed the same convergent–divergent nozzle, fed from a settling chamber and an impulsive injection device positioned upstream of the nozzle described in §2.1.1 (as sketched in Fig. 4).

At the start of each experiment, a steady swirl-free choked nozzle flow was established by using a Bronkhorst F-203AV linear resistance flow controller to impose a fixed axial mass-flow rate $\dot{m}_{\mathrm{ax}}$ of $1.194{\times}10^{-2}$ kg s^{-1} into a settling chamber ($V_{\mathrm{set}} = 10.5{\times}10^{-3}$ m^3) at temperature T_1. The pressure of the upstream reservoir was found to be $p_1 = 1.12$ bar (absolute). The imposed axial flow entered through a bell-mouth inlet a pipe section of length L_1 and radius R_1 upstream from a convergent–divergent nozzle, where $R_1 = 15$ mm and L_1 could either be set to: 220 mm or 340 mm. Under these flow conditions, there was a weak shock downstream from the nozzle throat [19,20].

The impulsive injection could be either radial or tangential and was performed at a distance of 85 mm upstream from the choked nozzle inlet. Tangential injection was aimed towards the nozzle inlet oriented at a 10° angle with respect to the normal to the main-flow direction (as sketched in Fig. 2 for the steady injection case). This was done to avoid a collision of the generated wall-bounded jet with itself, which is believed to occur when the injection is purely azimuthal. Radial injection took place trough the upstream pipe's center line at a 90° angle with respect to the choked nozzle axis. The impulsively injected mass-flow rate $\dot{m}_{\mathrm{imp}}$ was calibrated by means of a static calibration procedure succinctly described in §2.1.1 and in detail in Refs. [13,16]. The injection reservoir, $V_{\mathrm{imp}} = 2.8 \times 10^{-3}$ m^3, could be heated by means of an electric hot plate to a temperature T_{imp}.

The temperatures in the heated impulsive-injection reservoir T_{imp} and the upstream settling chamber T_1 were measured by using a Newport-Omega PT100 resistance thermometer. The tube connecting the impulsive-injection reservoir and the fast-switching valve had an internal diameter of 10 mm. When radial injection was performed, the tube was 150 mm long for tangential injection it was 15 mm long. The time delay for transfer of the heated air from the impulsive-injection reservoir to the injection port was estimated to be 60 ms for radial injection and 6 ms for tangential injection.

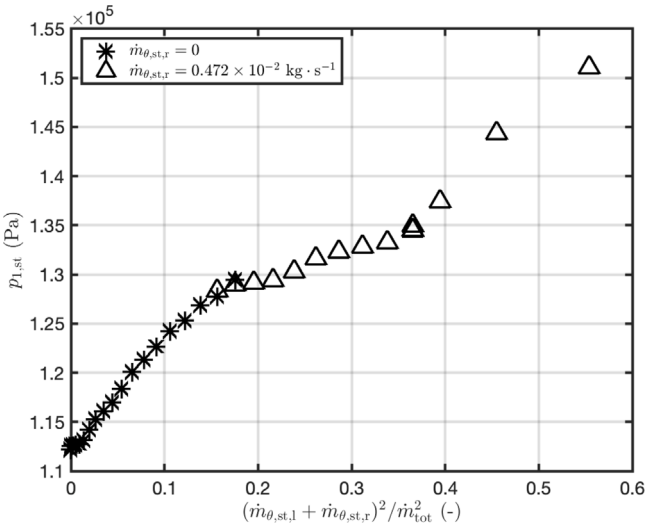

Fig. 5. Influence of $(\dot{m}_{\theta,st,l} + \dot{m}_{\theta,st,r})^2/\dot{m}_{tot}^2$ on $p_{1,st}$ where $\dot{m}_{tot} = 1.194 \times 10^{-2}$ kg s^{-1}.

Impulsive injections were performed once per second, ten times in a row. The one second interval was chosen because it is too short to allow cooling of the air in the tube connecting the impulsive-injection reservoir and the fast-switching valve. To ensure impulsive injection of heated air, ten additional injections were performed to preheat the fast-switching valve and the tube connecting the impulsive-injection reservoir before the start of the ten recorded events. The results were phase averaged, using a procedure described in Ref. [11]. The averaged signal was then passed through a low-pass filter with a cut-off frequency of $f_c = 234$ Hz.

3. Swirl–nozzle interaction experiment: results and analysis

3.1. Steady-flow measurements and quasi-steady models

In this section the use of steady-state measurements to construct quasi-steady models for the prediction of the downstream measured acoustic response amplitude, $|\Delta p'_{2,QSM}|$, is discussed. Two series of measurements were used:

A Steady-state measurements with a single steady tangential-injection port as described in §3.1.1. These measurements were used to model the downstream acoustic response due to swirl ingestion and evacuation in the case of a swirl-free background flow.

B Steady-state measurements with two steady tangential-injection ports as described in §3.1.2. These measurements were used to model the downstream acoustic response due to swirl perturbations of a swirl choked-nozzle flow with a steady background swirl.

Details of the experimental setup are discussed in §2.1.2.

3.1.1. Swirl-free background flow: one steady tangential-injection port

While keeping $\dot{m}_{\theta,st,r} = 0$ the steady tangential mass-flow rate trough the left-hand injection port (Fig. 3) $\dot{m}_{\theta,st,l}$ was varied – such that the sum of the steady axial mass-flow rate and steady tangential mass-flow rate was kept constant: $\dot{m}_{tot} = \dot{m}_{ax} + \dot{m}_{\theta,st,l} = 43.0$ kg h^{-1} $= 1.194 \times 10^{-2}$ kg s^{-1}. In Fig. 5, the steady-flow measurements of $p_{1,st}$ as a function of $\dot{m}_{\theta,st,l}/\dot{m}_{ax}$ are shown as stars.

In what follows, a model is proposed which uses the steady-state measurement data $p_{1,st}$, measured at constant $\dot{m}_{tot} = \dot{m}_{ax} + \dot{m}_{\theta,st,l}$, to predict the amplitude of the downstream acoustic response due to unsteady swirl–nozzle interaction for the case of a swirl-free background flow. A step-by-step derivation of this model, is provided by Hirschberg et al. [31]. In the absence of swirl, a steady frictionless quasi one-dimensional model for the axial mass-flow rate of a choked nozzle $\dot{m}^*_{ax}$ is:

$$\dot{m}^*_{ax} = A^*_{th} \frac{\gamma p_{1,BSF}}{c_1} \left(\frac{2}{\gamma + 1} \right)^{[\gamma+1]/[2(\gamma-1)]} \tag{3}$$

where A^*_{th} is the effective critical cross-sectional area of the nozzle throat, $p_{1,BSF}$ the upstream-reservoir pressure in the absence of swirl and c_1 the upstream sound speed. The change in axial mass-flow rate, $\Delta\dot{m}_{ax}$, due to the presence of swirl is then posited to be :

$$\Delta\dot{m}_{ax} = -A^*_{th} \frac{\gamma(p_{1,st} - p_{1,BSF})}{c_1} \left(\frac{2}{\gamma + 1} \right)^{[\gamma+1]/[2(\gamma-1)]} \tag{4}$$

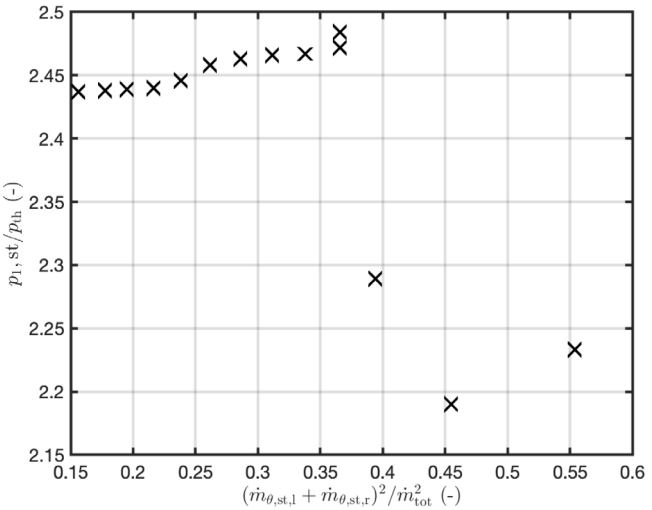

Fig. 6. Measured ratio $p_{1,\mathrm{st}}/p_{\mathrm{th}}$ of steady reservoir pressure to throat pressure as a function of the tangential injection mass-flow rate.

where $p_{1,\mathrm{st}}$ is the steady-state value of the upstream reservoir pressure in the presence of permanent swirl at fixed $\dot{m}_{\mathrm{ax}}$ (note that $p_{1,\mathrm{st}} > p_{1,\mathrm{BSF}}$). A change in axial mass-flow rate will drive a downstream-traveling acoustic wave, which in linear approximation, and assuming anechoic downstream boundary conditions, (simple-wave model) has the amplitude:

$$\Delta p'_{2,\mathrm{QSM}} \simeq \frac{c_2 \Delta \dot{m}_{\mathrm{ax}}}{A_2} \tag{5}$$

were $\Delta\dot{m}_{\mathrm{ax}}$ is determined using Eq. (4). The amplitude of the downstream-acoustic response, $\Delta p'_2$, due to either the ingestion ($\Delta\dot{m}_{\mathrm{ax}} < 0$) or evacuation ($\Delta\dot{m}_{\mathrm{ax}} > 0$) of swirl can be predicted using Eq. (5).

3.1.2. Perturbed steady background-swirl flow: two steady tangential-injection ports

In order to formulate a quasi-steady model to predict $\Delta p'_2$ due to the perturbation of a steady-background swirl passing through a choked nozzle, two tangential upstream injection ports were used. The first of these injected from the left-hand and the other from the right-hand side with respect to the direction of the flow. Steady tangential mass-flow rates through the left-hand, $\dot{m}_{\theta,\mathrm{st,l}}$ and right-hand, $\dot{m}_{\theta,\mathrm{st,r}}$, injection ports were established and controlled independently using Bronkhorst F-203AV linear resistance flow meters. Again, this was done while keeping $\dot{m}_{\mathrm{tot}}$ fixed at 1.194×10^{-2} kg s^{-1}; viz., $\dot{m}_{\mathrm{tot}} = \dot{m}_{\theta,\mathrm{st,r}} + \dot{m}_{\theta,\mathrm{st,l}} + \dot{m}_{\mathrm{ax}} = 1.194\times10^{-2}$ kg s^{-1}. In the experiments $\dot{m}_{\theta,\mathrm{st,r}} = 0.47\times10^{-2}$ kg s^{-1}, while $\dot{m}_{\theta,\mathrm{st,l}}$ was varied in the range $0 \le \dot{m}_{\theta,\mathrm{st,l}} \le 0.47\times10^{-2}$ kg s^{-1}. The triangles in Fig. 5 represent the values of p_1 obtained while varying the tangential mass-flow rates.

Hirschberg et al. [16], reported fits of steady-state swirling flow data for varied $\dot{m}_{\mathrm{tot}}$. Fig. 4 in Ref. [16], which shows $p_{1,\mathrm{st}}$ as a function of $\dot{m}_{\theta,\mathrm{st}}/\dot{m}_{\mathrm{ax}}$, demonstrates that the correlations for the various $\dot{m}_{\mathrm{tot}}$ are similar except that they shift in the positive direction of the vertical axis as $\dot{m}_{\mathrm{tot}}$ is increased. Moreover, the magnitude of the shift in $p_{1,\mathrm{st}}$ appears to be linear function of $\dot{m}_{\mathrm{tot}}$.

Thus, the difference between the upstream pressure $p_{1,\mathrm{st}}$ due to a change in swirl and the upstream pressure $p_{1,\mathrm{RSO}}$ which occurs with steady tangential injection through the right-hand port only: $p_{1,\mathrm{st}} - p_{1,\mathrm{RSO}}$, is taken to be a measure for the axial mass-flow rate change, $\Delta\dot{m}_{\mathrm{ax}}$, induced by the change in upstream tangential injection through the left-hand side port:

$$\Delta\dot{m}_{\mathrm{ax}} = -A^*_{\mathrm{th}} \frac{\gamma(p_{1,\mathrm{st}} - p_{1,\mathrm{RSO}})}{c_1} \left(\frac{2}{\gamma+1}\right)^{[\gamma+1]/[2(\gamma-1)]} \tag{6}$$

As in the background-swirl free case such a change in axial mass-flow rate will drive a downstream-traveling acoustic wave, the amplitude of which can be estimated with Eq. (5).

Note that there is a change in slope of the relation between $p_{1,\mathrm{st}}$ and $(\dot{m}_{\theta,\mathrm{st,r}} + \dot{m}_{\theta,\mathrm{st,l}})/\dot{m}_{\mathrm{ax}}$ in Fig. 5 when the second tangential injection port begins to be used. Moreover, a second change in slope is observed around $(\dot{m}_{\theta,\mathrm{st,l}} + \dot{m}_{\theta,\mathrm{st,r}})^2/\dot{m}^2_{\mathrm{tot}} = 0.38$, which indicates a transition in flow behavior. This indicates that simply adding the two tangentially-injected mass flows is a rudimentary assumption.

3.1.3. Estimation of azimuthal velocity at the nozzle inlet

In addition to $p_{1,\mathrm{st}}$, the static pressure at the nozzle throat, p_{th} was measured. As explained in Appendix A, this makes the estimation of the Mach number M_{th} close to the wall at the throat possible. Using as input the measured pressure ratio p_1/p_{th} displayed in Fig. 6, this azimuthal velocity is estimated to be of the order of $u_{\theta,\mathrm{in}} \simeq 50$ m s^{-1}. This is much larger than the axial velocity $u_{\mathrm{x,in}} = 12.5$ m s^{-1}. Note the sudden change in flow behavior observed around $(\dot{m}_{\theta,\mathrm{st,l}} + \dot{m}_{\theta,\mathrm{st,r}})^2/\dot{m}^2_{\mathrm{tot}} = 0.38$ in Fig. 6, which was already noticed in Fig. 5.

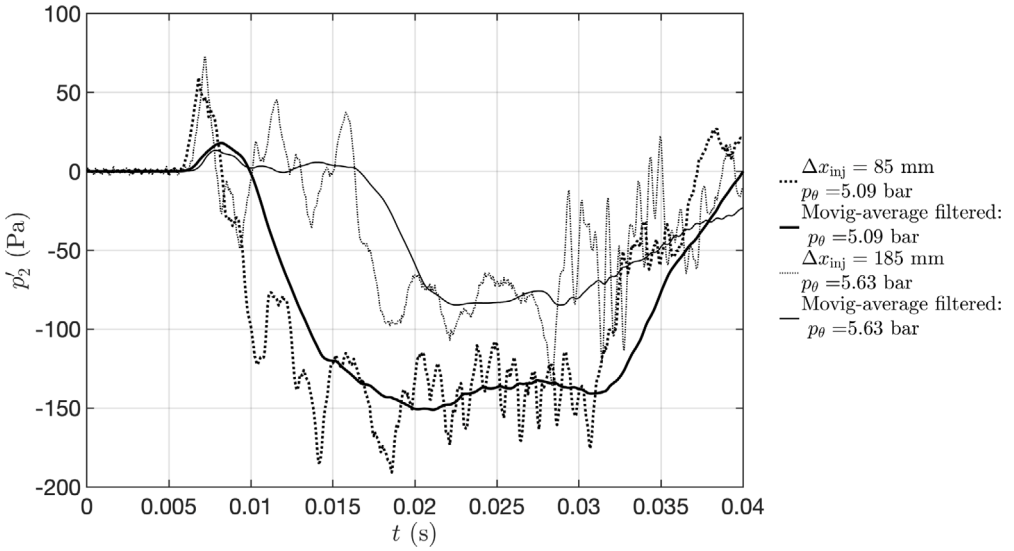

Fig. 7. Downstream pressure fluctuations p_2' – measured 1150 mm downstream of the nozzle throat – as function of the time t, for two tangential-injection distances $\Delta x_{\rm inj}$ upstream from the nozzle inlet. The phase-averaged signal p_2' over 100 consecutive experiments displays direct-sound oscillations due to the upstream-pipe quarter-wavelength oscillation. These oscillations are eliminated in the moving-averaged signal. The trigger time used to open and close the valve was identical in both measurements: $\tau_{\rm valve} = 10$ ms.

3.2. Direct and indirect noise

3.2.1. Influence of the position of the injection port on upstream and downstream acoustic signals

In Fig. 7, two typical results – obtained with two different distances $\Delta x_{\rm inj}$ between the tangential injection point and the nozzle inlet; viz., $\Delta x_{\rm inj} = 85$ mm and $\Delta x_{\rm inj} = 185$ mm – of the downstream pressure variation p_2' as a function of time t elapsed after the trigger-opening signal for the fast-switching injection valve. In both cases the axial injection mass-flow rate is $\dot{m}_{\rm ax} = 1.194\times10^{-2}$ kg s^{-1}. This imposed axial mass-flow rate establishes an initial upstream pressure of $p_1 = 1.12$ bar and an axial mean-flow velocity $U_1 = 12.5$ m s^{-1} at the nozzle inlet. Moreover, the trigger signal used to open and close the valve was identical in both measurements: $\tau_{\rm valve} = 10$ ms.

In Fig. 7, both the original phase-averaged microphone signals (averaged over a 100 injection events) are shown as dotted lines. To these signals a moving-average filter was applied to remove the quarter wave-length oscillations of the upstream pipe segment triggered by the onset of tangential injection. The resulting low-pass filtered signals are shown as solid lines in Fig. 7.

Measurement, shown in Fig. 8, of the upstream pressure p_1' – performed with a microphone placed 266 mm upstream from the nozzle – demonstrate (as had already been established in Refs. [13,16]) that the valve opens with a delay of 2.5 ms after the electrical-trigger signal at $t = 0$. The injection reservoir pressure was $p_\theta = 5.09$ bar (absolute) – for the injection at $\Delta x_{\rm inj} = 85$ mm – which corresponds to a steady mass-flow rate of $\dot{m}_\theta \simeq 3.39\times10^{-3}$ kg s^{-1}. When injected in an infinitely extended pipe this would induce an upstream-traveling wave p_1^- and a downstream-traveling wave p_1^+ with amplitudes $|p_1^+| = |p_1^-| = \dot{m}_\theta c_1/(2\pi R_1^2) \simeq 823$ Pa — where the convection due to the main flow velocity $U_1 = 12.5$ m s^{-1} has been neglected and the $c_1 = 343$ m s^{-1} was used. The measurement of p_1' shows a pressure peak of 720 Pa at $t = 3.5$ ms, this indicates that the valve-opening time is of the order of 1 ms. The upstream compression waves reflects as an expansion wave at the transition of the pipe with the reservoir $x = -340$ mm (where the nozzle inlet is at $x = 0$). Taking into account an end-correction of $R_1 = 15$ mm, this expansion wave reaches the microphone 0.5 ms after passage of the initial compression wave. This results in an abrupt decrease of p_1'. Almost concurrently, the reflection of the downstream compression wave at nozzle inlet reaches the microphone.

Using a quasi-steady flow approximation one can predict the reflection coefficient of waves at the nozzle. Details are provided in Appendix B. One finds a reflection coefficient $r_{\rm nozzle} = 0.986$. This implies a pressure peak at the nozzle inlet of amplitude $p_1' = p_1^+(1 + r_{\rm nozzle}) = 1634$ Pa. Ergo, in first order approximation the nozzle behaves as a closed pipe termination. The inlet of the pipe at the reservoir behaves approximately as an open pipe termination. Therefore, the acoustic perturbation initiated by the sudden injection upstream of the nozzle is dominated by the quarter wavelength of the pipe joining the reservoir to the nozzle. This oscillation has a frequency of ca. $c_1/[4(L_1 + R_1)] = 242$ Hz (where $L_1 = 340$ mm).

3.2.2. Transmission of initial pressure pulse through the nozzle

Using the quasi-steady-one dimensional approximation described in Appendix C for the amplitude $p_1' = 1634$ Pa at the nozzle inlet, one finds a transmission-wave amplitude $p_2' = 47$ Pa. This wave should reach the downstream microphone – located 1150 mm downstream from the nozzle throat – with a delay of the order of 3 ms after the opening of the valve at $t = 2.5$ ms. Indeed, at about $t = 5.5$ ms, one observes in Fig. 7 a sudden increase of p_2'. In the experiments the measured amplitude of the first peak is $p_2' = 60$ Pa. This confirms that the observed first peak in p_2' corresponds to direct sound transmission through the nozzle.

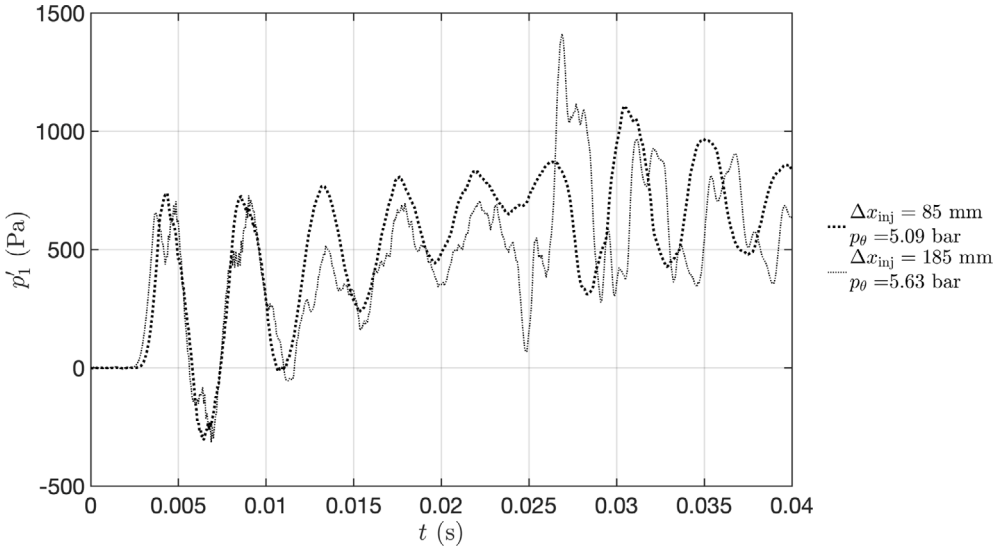

Fig. 8. Upstream acoustic pressure signal p_1' vs. time t. p_1' is phase-averaged result of 100 consecutive injection events. Two results are shown, obtained with two different injection port positions, Δx_{inj}, and injection reservoir pressures p_θ. The trigger time used to open and close the valve was identical in both measurements: $\tau_{\mathrm{valve}} = 10$ ms.

3.2.3. Vortex-ingestion and vortex-evacuation signals

The signal, in Fig. 7, found for injection at $\Delta x_{\mathrm{inj}} = 185$ mm is initially very similar to that for $\Delta x_{\mathrm{inj}} = 85$ mm. However around $t = 9.5$ ms the two signals diverge drastically. Until $t = 17.0$ ms, the signal for $\Delta x_{\mathrm{inj}} = 185$ mm displays oscillations around $p_2' = 0$ corresponding to the 242 Hz upstream-pipe quarter-wavelength oscillation. After $t = 17.0$ ms, p_2' decreases abruptly. Whereas, the signal for $\Delta x_{\mathrm{inj}} = 85$ mm already decreases abruptly at $t = 9.5$ ms. The sudden decrease in p_2' is assumed to be due to the arrival and intake of the swirl (axial vortex) at the nozzle. In this text, this is going forward referred to as the "ingestion" of the axial vortex/swirl. The observed delay of 7.5 ms between the occurrence of ingestion, due to the 100 mm difference in distance from tangential injection point to nozzle inlet, clearly corresponds to the convection time of 8 ms with flow velocity $U_1 = 12.5$ m s^{-1} over 100 mm. We note, that for $\Delta x_{\mathrm{inj}} = 85$ mm, the delay of 4 ms between the first direct-sound pulse at $t = 5.5$ ms and the decrease of p_2' at $t = 9.5$ ms, due to swirl ingestion is shorter than a convection time of 7 ms for a velocity $U_1 = 12.5$ m s^{-1}. This difference in delay, between the valve opening and the swirl ingestion is a first hint of the complex flow behavior that will be noted in other experiments.

To rule out that this is entropy noise consider the flowing:

- Both the main axial air flow and the tangentially-injected air flow are originate in reservoirs at room temperature and an absolute pressure of 6 bar. The Joule–Thomson effect is, the same for both streams and very minor: ca. −1 K.
- A source of entropy difference will be the heating of the cold high speed flow in the short pipe segment between the fast-switching valve and the injection nozzle. As this tangentially injected air reaches the nozzle inlet it will have a slightly higher total temperature than the main axial flow. This can certainly not explain a decrease in p_2'.
- One could argue that this tangentially-injected air has a higher speed compared to the main flow when it reaches the nozzle and is therefore colder. This might explain a decrease in p_2'. However, as will later (§4) be demonstrated experimentally by means of tangentially injecting heated air the tangentially-injected: the injected fluid only reaches the nozzle around $t = 20$ ms.

Ergo, the sudden decrease in p_2' at $t = 9.5$ ms is certainly not related to entropy noise.

In Fig. 7, one notes that the decrease in p_2' due to swirl ingestion is for $\Delta x_{\mathrm{inj}} = 185$ ms significantly smaller than for $\Delta x_{\mathrm{inj}} = 85$ mm. As explained by Hirschberg et al. [21], the reduction of indirect-sound signal amplitude with increasing injection distance Δx_{inj}, is due to the decay of the swirl caused by wall friction.

One notes, in Fig. 7, after the sudden decrease due to the ingestion of the swirl the pressure p_2' oscillates – as a result of direct sound due to the quarter-wavelength upstream resonance – around a constant value until the upstream tangential injection is interrupted. The interruption of the injection generates a sharp negative direct sound pulse, which arrives at the downstream microphone: at $t = 30.5$ ms for $x = -85$ mm and at $t = 28.0$ ms for $\Delta x_{\mathrm{inj}} = 185$ mm, respectively. The amplitude of these peaks is comparable to that of the direct-sound pulse at the onset of tangential injection. The delay of the order of 20 ms indicates a slow reaction of the valve to the electrical trigger for closing. After this pulse, one observes an increase which is due to the clearance of the swirl out of the nozzle. This phase is going forward referred to as the axial vortex/swirl "evacuation" phase. It will be seen, that after a sudden initial positive jump in p_2', this increase is relatively gradual. Moreover, in the following it will shown that the total increase in p_2' due to evacuation is larger than the decrease upon ingestion.

It is convenient – for the purpose of comparison between different measurements – to filter out the direct-sound signal due to the upstream quarter-wavelength oscillation. Therefore, in the following the acoustic signals will be low-pass filtered as shown in Fig. 7 (the solid lines).

3.3. Response in absence of permanent swirl

3.3.1. Effect of tilting angle of tangential injection and injection time

In Fig. 9 a typical downstream recorded acoustic pressure signal, p_2', resulting from upstream unsteady-tangential injection into a swirl-free background flow is shown as a function of the time. The swirl-free background flow was established by imposing an axial mass-flow rate of $\dot{m}_{ax} = 1.194 \times 10^{-2}$ kg s^{-1}. Unsteady-tangential injection was performed though the left-hand side injection port, resulting in a tangential mass-flow rate $\dot{m}_{\theta,l}$. Data was obtained using one of the two following tangential-injection angles ϕ_θ: $\phi_\theta = 0°$ (perpendicular to the axial flow), or at a $\phi_\theta = 10°$ relative to the perpendicular direction. The results were obtained with various fast-switching trigger times τ_{valve} and with an absolute injection-reservoir pressure $p_\theta = 6.2$ bar ($\dot{m}_{\theta,l} = 0.417 \times 10^{-2}$ kg s^{-1}). The upstream pipe length used was $L_1 = 340$ mm.

In both cases, one observes the relatively small positive-pressure peak at $t \simeq 8$ ms due to the acoustic pressure pulse generated in the upstream pipe by the opening of the fast-switching valve (Section 3.2). This pulse is partially transmitted through the nozzle, resulting in a direct-sound pulse. The direct-sound pulse is almost immediately followed by an abrupt step-wise decrease of negative amplitude ($\Delta p_2' < 0$) in p_2'. This is due to the ingestion of swirl by the choked nozzle. Shortly after the valve is closed, the swirl is evacuated from the nozzle throat and one observes an upwards step in p_2' of positive amplitude ($\Delta p_2' > 0$). Note that in Fig. 9, p_2' is polluted by upstream-traveling reflections for $t > 150$ ms. Furthermore, the authors note that the interpretation of these measurements is complicated by the limited low-frequency response of the microphone. After 20 ms, an initially constant plateau in p_2' starts deviating significantly [16].

The main difference between p_2' obtained with the $\phi_\theta = 0°$ and $\phi_\theta = 10°$ configurations is an additional oscillation for $\phi_\theta = 10°$ when the valve is closed. This phenomenon is not yet understood. It will not be considered during the further analysis as it does not significantly affect the magnitude of the pressure decrease. Consequently, it is presumed that the indirect-sound contribution to p_2' is not affected by the tilting of the injection nozzle.

The amplitude $|\Delta p_2'|$ of the initial decrease in p_2' due to swirl ingestion is observed to be smaller than that of the increase in p_2' due to swirl evacuation. In the following the authors discuss two effects which in their view play a role in this observation.

1. Hot-wire measurements by Kings (Fig. A.21 (e) in Ref. [12]) of the azimuthal velocity downstream from the injection point – 58 mm upstream from the nozzle – showed that about 30 ms after the start of the tangential injection, the flow was dominated by a thin wall-bounded jet. This wall-bounded jet is only partially visible, as it occurred in a region of less than 3 mm from the pipe wall which was not accessible to the hot wire. The authors note that 70 ms after the opening of the valve, Kings' hot-wire measurements (Fig. A.21 (f) in Ref. [12]) display a much more uniform azimuthal velocity. The authors also note that the data shown in figure 5.22 (b) of Ref. [12] obtained 50 ms after tangential injection was initiated show a velocity profile approaching that of a "forced vortex" (viscous-dominated "solid" rotation). In summary, the swirl structure evolves with time.
2. In this set of experiments an under-expanded sonic jet is injected azimuthally into a swirl-free flow of mean velocity $U_1 = 12.5$ m s^{-1}. Therefore, one expects the resulting high-speed wall-bounded jet to make one revolution and return to the injection point (the authors are quite confident that this occurs for $\phi_\theta = 0°$). The interaction of the wall-bounded jet with itself likely causes a split into two helicoidally flowing components: one flowing towards the nozzle inlet and the other flowing upstream towards the settling chamber. Furthermore, there is only a slow increase in the settling-chamber pressure p_1. The time constant for the increase in settling chamber pressure p_1 due to an unsteady tangential-injection mass-flow rate $\dot{m}_\theta$ is $(\rho_1 V_{set})/(\gamma \dot{m}_\theta)$. For the highest values of $\dot{m}_\theta = 3.3 \times 10^{-3}$ kg s^{-1}, this is 3 s. The unsteady injection is shorter than 0.1 s. This implies that the choked nozzle cannot absorb the supplementary unsteady-mass injection. Thus, only part of the injected swirl would be initially ingested by the choked nozzle. It is speculated that part of the jet traveling upstream will result in an accumulation of swirl upstream from the nozzle which is evacuated through the nozzle after the unsteady-tangential injection is halted. I.e., more swirl would be evacuated than was initially ingested (just after the start of the unsteady tangential injection). Hence, a larger $|\Delta p_2'|$ due to the evacuation of swirl can be expected. In support of this hypothesis, the authors note that $|\Delta p_2'|$ due to swirl evacuation depends on the duration of the valve opening [16].

3.3.2. Comparison with semi-empirical model

In Fig. 10, the dimensionless amplitude of the acoustic signal $|\Delta p_2'|\rho_2 \left(\pi R_2^2\right)^2/(\dot{m}_{\theta,l})^2$, obtained with the tilted ($\phi_\theta = 10°$) tangential-injection nozzle, is shown as a function of $\left(\dot{m}_{\theta,l}/\dot{m}_{ax}\right)^2$ for $\tau_{valve} = 50$ ms. The data for swirl evacuation agrees quantitatively with the prediction of the empirical quasi-steady model; viz. Eq. (5) for $\Delta p_{2,QSM}'$ in combination with Eq. (4)) as described in §3.1.1. We note that – as $|\Delta p_2'|$ due to swirl evacuation depends on the injection time (the length of time the valve during which the valve is opened) [16] – this excellent agreement is partially due to the particular choice of injection time considered here. However, the quasi-steady theory predicts the experimental results with deviations less than 50%. The effect of swirl ingestion is systematically lower than that of evacuation – by about 30% – but follows the same quadratic scaling rule. This confirms that part of the tangentially-injected fluid flows upstream from the injection point. These results confirm for the case of a swirl-free background flow that in first-order approximation $|\Delta p_2'|_{BSF}$ is proportional to $\dot{m}_{\theta,l}^2$ [16].

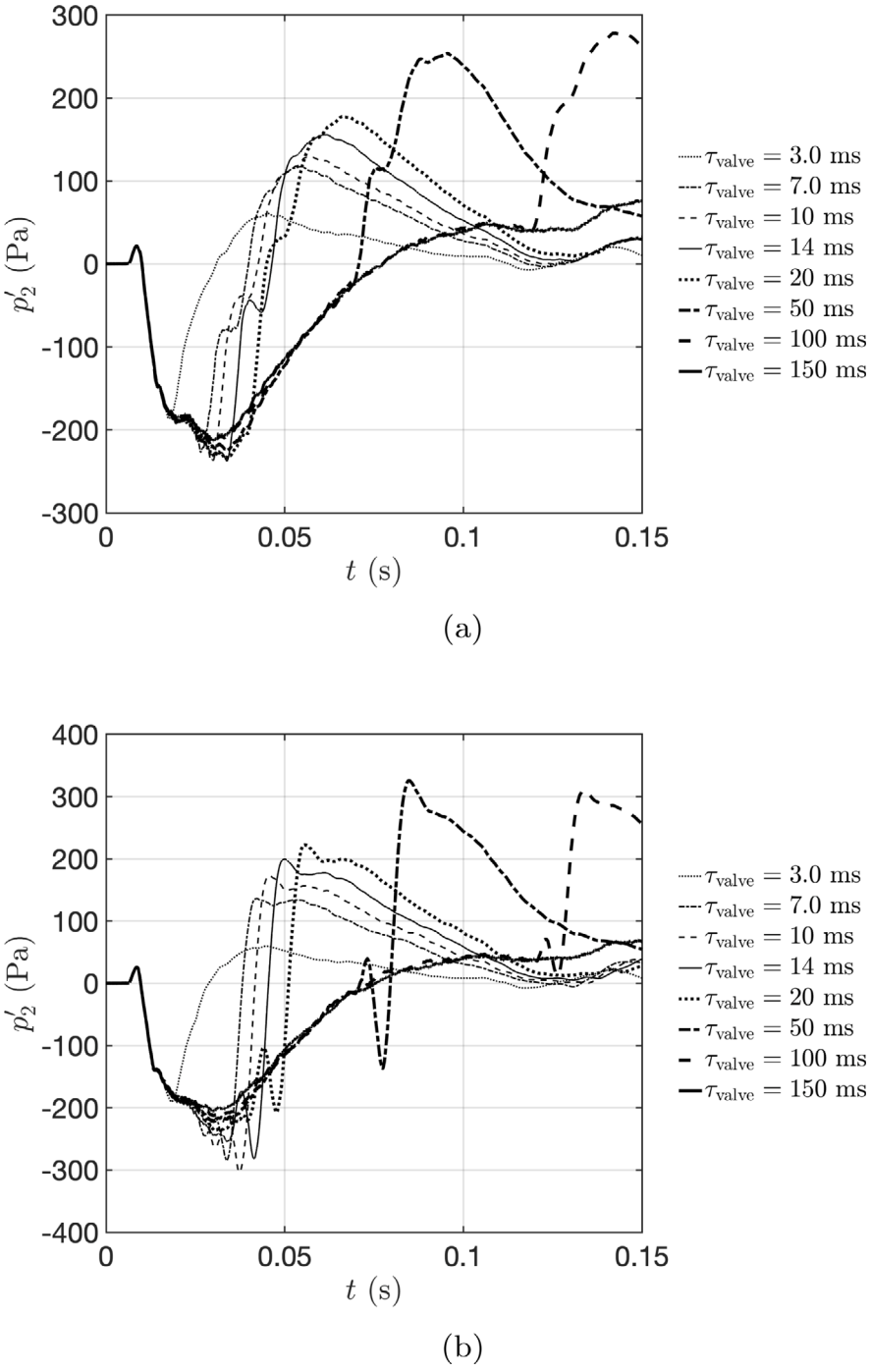

Fig. 9. p_2' for $\dot{m}_{\theta,J} = 0.417 \times 10^{-2}$ kg s^{-1} into a swirl-free background flow, for varied τ_{valve}. (a) $\phi_\theta = 0°$ (b) $\phi_\theta = 10°$.

3.4. Perturbation of a low-intensity background swirl on the downstream acoustic response

In Fig. 11, p_2' due to the perturbation of a flow with a steady low-intensity background swirl is presented. The upstream pipe-section length L_1 used to obtain the results was 220 mm. A steady-state was established fixing the axial mass-flow rate to $\dot{m}_{\text{ax}} = 1.00 \times 10^{-2}$ kg s^{-1} while performing steady tangential injection with $\dot{m}_{\theta,\text{st,r}} = 1.94 \times 10^{-3}$ kg s^{-1} at a location $\Delta x_{\text{inj}} = 85$ mm using an injection port with $\phi_\theta = 10°$. This low-intensity background swirl flow was perturbed by means of additional tangential injections with $\tau_{\text{valve}} = 70$ ms at various p_θ.

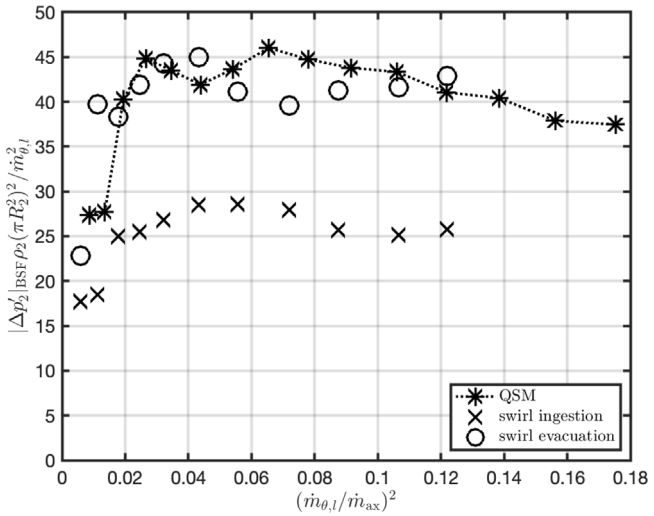

Fig. 10. Dimensionless $\Delta p_2'$ due to either the ingestion (crosses) or evacuation (circles) of swirl compared to QSM prediction (dotted-line connected stars). Results obtained with $\tau_{\mathrm{valve}} = 50$ ms.

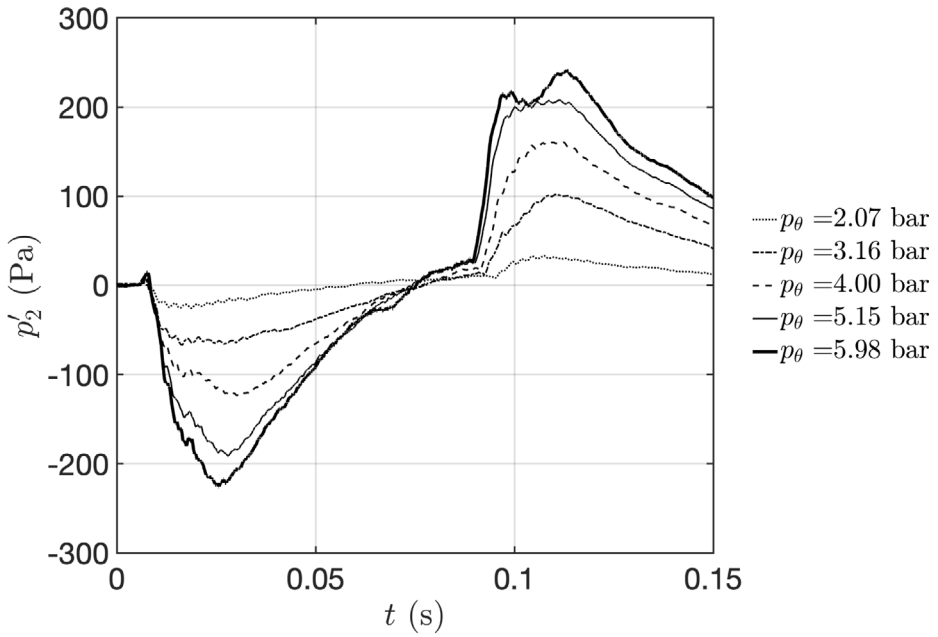

Fig. 11. p_2' due to the perturbation of low-intensity steady-background swirl, for $\dot{m}_{\mathrm{ax}} = 1.00 \times 10^{-2}$ kg s^{-1}, $\dot{m}_{\theta,\mathrm{st,r}} = 1.94 \times 10^{-3}$ kg s^{-1} and $\tau_{\mathrm{valve}} = 70$ ms.

Comparison with results obtained without background swirl (Fig. 9) shows the low-intensity background swirl has a minor effect on $|\Delta p_2'|$. However, for $\phi_\theta = 10°$ one notes that the background swirl suppresses the unexplained oscillations in p_2' previously obtained when closing the fast-switching injection valve.

3.5. Perturbation of a high-intensity background swirl on the downstream acoustic response

In Fig. 12(a), p_2' resulting from the perturbation of a high-intensity steady background swirl is shown. The latter was established in a $L_1 = 340$ mm upstream tube with $\dot{m}_{\theta,\mathrm{st,r}} = 0.472 \times 10^{-2}$ kg s^{-1} and $\phi_\theta = 10°$. The high-intensity background swirl flow was perturbed by means of unsteady tangential injection with a fast-switching trigger time of $\tau_{\mathrm{valve}} = 10$ ms. The injection-reservoir pressure p_θ, and as such $\dot{m}_{\theta,\mathrm{st,r}}$, was varied. In Fig. 12(b), results obtained in absence of a steady-background swirl (i.e. $\dot{m}_{\theta,\mathrm{st,r}} = 0$ and $\dot{m}_{\mathrm{ax}} = 1.194 \times 10^{-2}$ kg s^{-1} kg s^{-1}), whilst leaving τ_{valve}, L_1, and ϕ_θ unaltered are shown for comparison. One notes that the

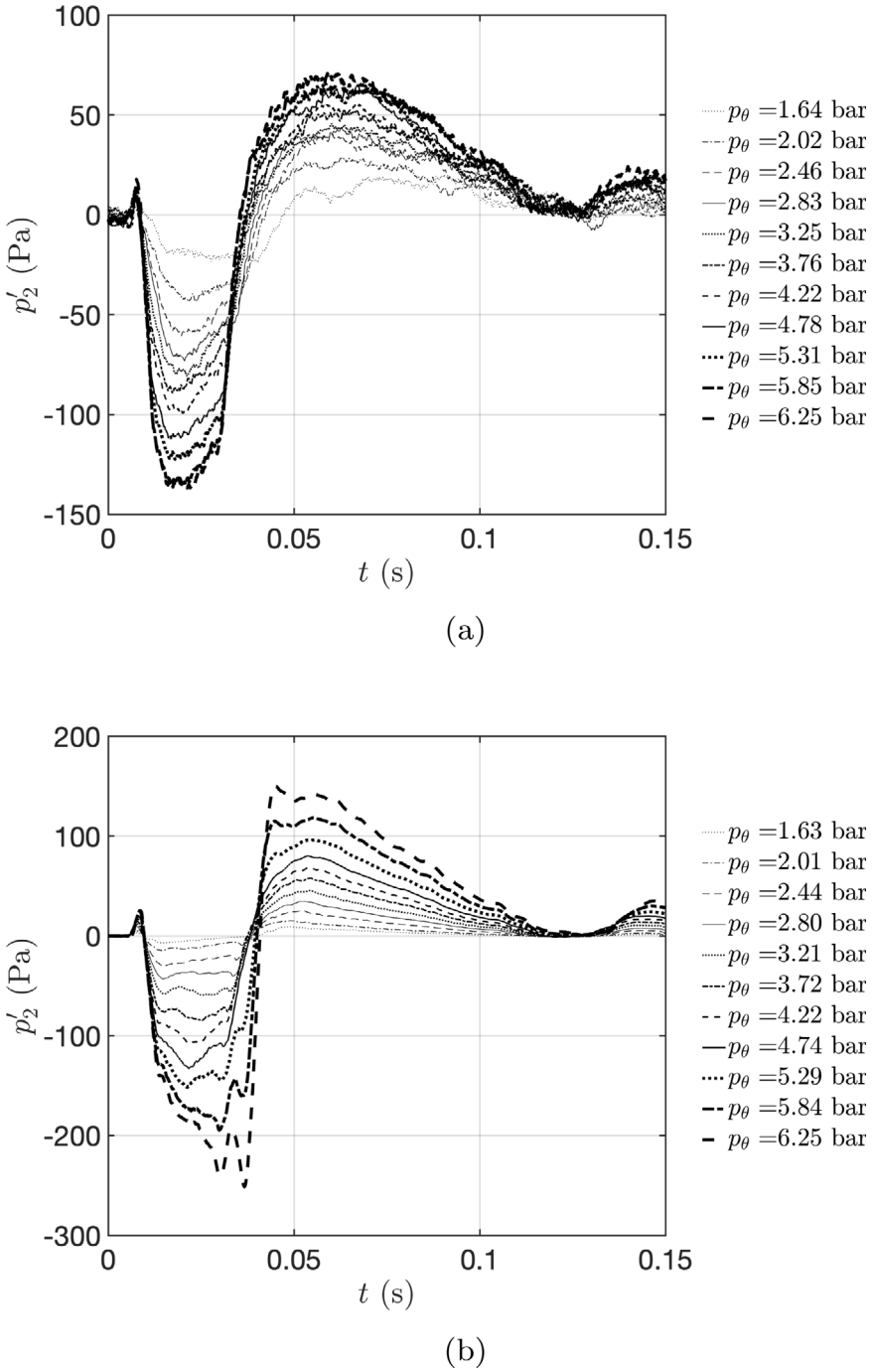

Fig. 12. Comparison of p_2' in presence (a) and absence (b) of a high-intensity background swirl. In both cases $\tau_{\text{valve}} = 10$ ms. (a) $\dot{m}_{\theta,\text{st,r}} = 0.472 \times 10^{-2}$ kg s^{-1} and $\dot{m}_{\text{ax}} = 0.722 \times 10^{-2}$ kg s^{-1} (b) $\dot{m}_{\theta,\text{st,r}} = 0$ and $\dot{m}_{\text{ax}} = 1.194 \times 10^{-2}$ kg s^{-1}.

oscillation believed to be due to the closing of the fast-switching valve is suppressed in the case of a high intensity background swirl flow. More quantitative analysis of these data is provided below.

In Fig. 13, $|\Delta p_2'|/|\Delta p_2'|_{\text{BSF}}$ is shown as a function of $\dot{m}_{\theta,\text{l}}/\dot{m}_{\theta,\text{st,r}}$; were $\Delta p_2'$ is the downstream recorded amplitude (Fig. 12(a) data) due to ingestion and evacuation of the high-intensity background-swirl perturbation. $\Delta p_2'$ is compared to $|\Delta p_2'|_{\text{BSF}}$, the steady background-swirl free data of Fig. 12(b). Notably, the ratio $|\Delta p_2'|/|\Delta p_2'|_{\text{BSF}}$ is the same for swirl ingestion and evacuation. One notes

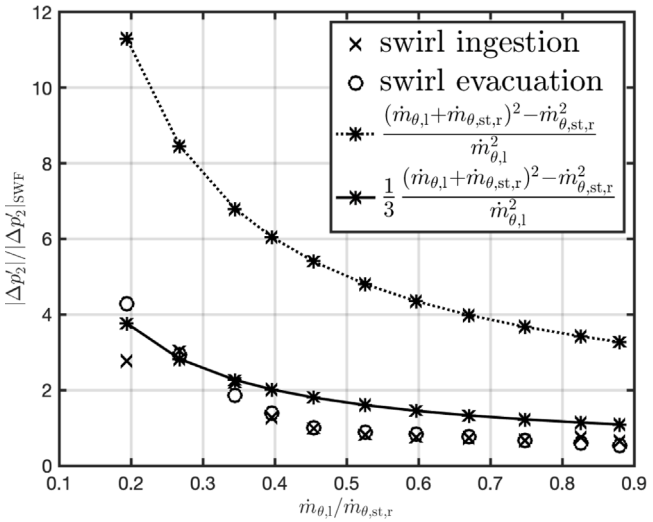

Fig. 13. Comparison of the response amplitude due to the perturbation of a high-intensity steady-background swirl to the background swirl-free case for $\tau_{\mathrm{valve}} = 10$ ms.

that for $\dot{m}_{\theta,\mathrm{l}}/\dot{m}_{\theta,\mathrm{st,r}} < 0.4$, the steady-background swirl amplifies $|\Delta p'_2|$. Whereas, for $\dot{m}_{\theta,l}/\dot{m}_{\theta,\mathrm{st,r}} > 0.5$, $|\Delta p'_2|$ is diminished by the presence of the steady background swirl.

In §3.4, it was noted that in the absence of background swirl:

$$|\Delta p'_2|_{\mathrm{BSF}} \propto \dot{m}^2_{\theta,\mathrm{l}}. \tag{7}$$

With that in mind, and assuming that the unsteady and steady swirl are additive while noting that a steady state does not produce sound, the authors posit that in the presence of a strong steady background swirl:

$$|\Delta p'_2| \propto (\dot{m}_{\theta,\mathrm{l}} + \dot{m}_{\theta,\mathrm{st,r}})^2 - \dot{m}^2_{\theta,\mathrm{st,r}}. \tag{8}$$

I.e., it is rationalized that in the experiment, coalescence of the two initially separated (left and right) tangentially injected flows occurs. N.b., Eq. (8) is the unsteady part of the summed tangential injections. For the ratio $|\Delta p'_2|/|\Delta p'_2|_{\mathrm{BSF}}$, one has the following scaling rule:

$$\frac{|\Delta p'_2|}{|\Delta p'_2|_{\mathrm{BSF}}} \propto \frac{(\dot{m}_{\theta,\mathrm{l}} + \dot{m}_{\theta,\mathrm{st,r}})^2 - \dot{m}^2_{\theta,\mathrm{st,r}}}{\dot{m}^2_{\theta,\mathrm{l}}}. \tag{9}$$

In Fig. 13, Eq. (9) is plotted (line-connected crosses). One observes the scaling rule provides an order of magnitude prediction. Indeed, dividing by three one recovers the dotted-line connected crosses. Keeping in mind the bare-bones nature of the scaling rule, its predictions compare remarkably well with the empirical data. Although Eq. (9) overestimates the effect of the permanent swirl by ca. a factor three, it reflects the decreasing trend of $|\Delta p'_2|/|\Delta p'_2|_{\mathrm{BSF}}$ with increasing $\dot{m}_{\theta,\mathrm{l}}/\dot{m}_{\theta,\mathrm{st,r}}$ observed in the empirical data. As it will be seen below from measurements with longer injection times, the relatively low response for short injection times is related to complex behavior of the flow upstream of the choked nozzle.

When the valve-trigger pulse time τ_{valve} is prolonged, an interesting effect is observed. This appears in Fig. 14, which shows results obtained for varying p_θ with $\tau_{\mathrm{valve}} = 70$ ms, $L_1 = 220$ mm, $\dot{m}_{\mathrm{ax}} = 8.61\times10^{-3}$ kg s^{-1}, and $\dot{m}_{\theta,\mathrm{st,r}} = 3.33\times10^{-3}$ kg s^{-1}. Between $t = 50$ ms and $t = 80$ ms, a negative large-amplitude peak appears, most notably for an unsteady-injection reservoir pressure $p_\theta = 6.24$ bar (thickest solid black line). Such a secondary negative peak (i.e. after the initial swirl-ingestion response) will be referred to as the second stage or stage 2 peak in this text. The amplitude of the stage 2 peak, $|\Delta p'_2|_{\mathrm{stage2}}$, was determined from the point where the response starts to appear and the point corresponding to a local minimum. For the thickest solid black line in Fig. 14, this occurs around $t = 45$ ms and 61 ms, respectively. The total ingestion response was defined as the sum of the first and second stage responses: $|\Delta p'_2| = |(\Delta p'_2)_{\mathrm{stage1}} + (\Delta p'_2)_{\mathrm{stage2}}|$. Those data are indicated by triangles in Fig. 15.

The authors hypothesize that the second stage pulse is related to the deflection of a significant part of the unsteady tangentially-injected mass flow in the upstream direction. In which case, at high injection mass-flow rates the associated swirl will accumulate upstream of the injection point. After a time – of the order-of-magnitude of the convection time along the upstream pipe $L_1/U_1 = 3\times10^1$ ms – an instability of this very complex flow occurs. This releases the accumulated swirl, which is ingested by the nozzle and a flow approaching a quasi-steady flow is established. The onset of the second stage almost coincides with the transition in flow from wall-bounded swirling jet to solid-body-like rotation observed by Kings (see figures A.10 and A.11 in [12]). This phenomenon is certainly relevant when considering swirl dynamics for the tuning of the thrust in a rocket engine upstream of the engine's choked nozzle.

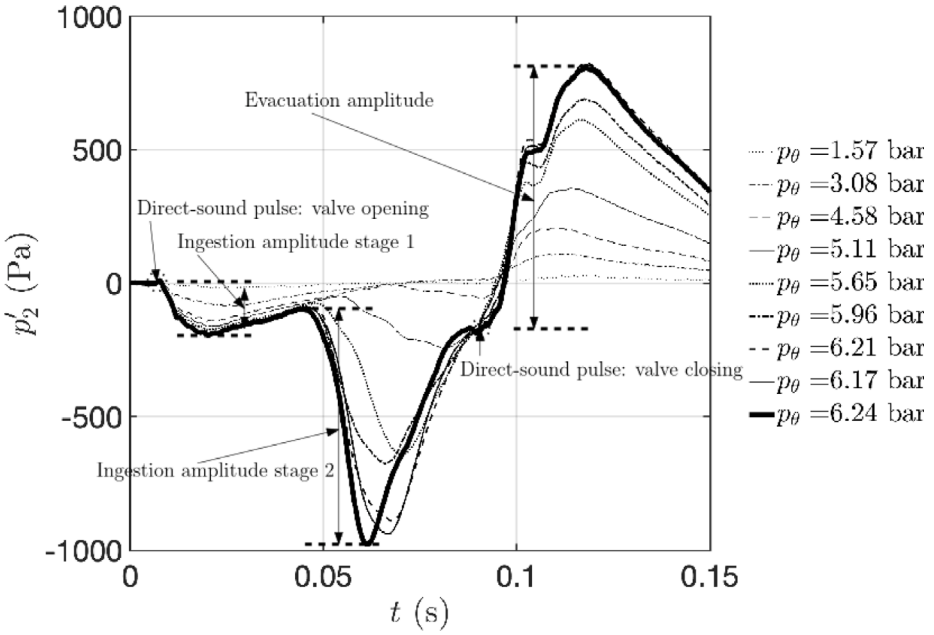

Fig. 14. p_2' displaying a pronounced second stage peak for $\tau_{\text{valve}} = 70$ ms and high-intensity background swirl.

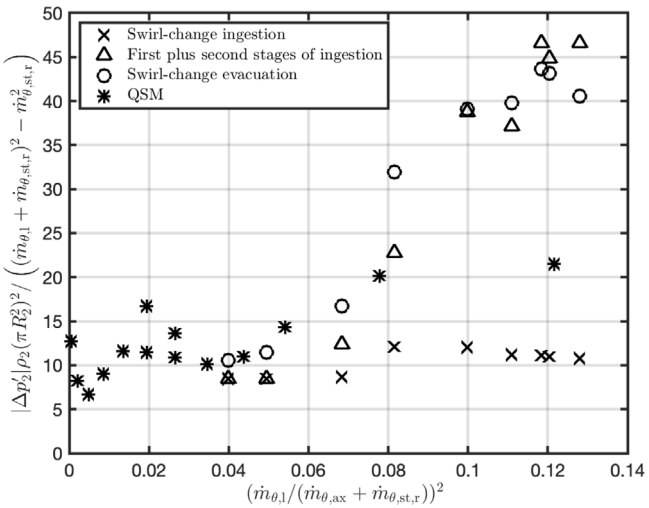

Fig. 15. $\Delta p_2'$ due to first stage swirl-change ingestion (crosses), first plus second stages of ingestion (triangles), swirl-change evacuation (circles). Empirical data are compared to the QSM predictions (stars).

The amplitudes observed in Fig. 14 were scaled using Eq. (8) to produce Fig. 15. In this figure the dimensionless amplitudes, $|\Delta p_2'|\rho_2\left(\pi R_2^2\right)^2/((\dot{m}_{\theta,1}+\dot{m}_{\theta,\text{st,r}})^2-\dot{m}_{\theta,\text{st,r}}^2)$, are shown as a function of $(\dot{m}_{\theta,1}/(\dot{m}_{\text{ax}}+\dot{m}_{\theta,\text{st,r}}))^2$; the acoustic response due to: first stage ingestion, first plus second stage ingestion, and swirl-change evacuation are indicated by crosses, triangles and circles, respectively.

Interestingly, for $(\dot{m}_{\theta,1}/(\dot{m}_{\text{ax}}+\dot{m}_{\theta,\text{st,r}}))^2 > 0.08$, both the amplitudes due to swirl-change evacuation and the first stage plus second stage ingestion response reached ca. 45; which, as can be appreciated in Fig. 10, is about the same numerical value obtained in the absence of a steady-background swirl.

The authors note that for $(\dot{m}_{\theta,1}/(\dot{m}_{\text{ax}}+\dot{m}_{\theta,\text{st,r}}))^2 < 0.08$ and $\dot{m}_{\theta,1}/\dot{m}_{\theta,\text{st,r}} = O(1)$, which is the case for the data in Fig. 15, the quasi-steady model (QSM; see §3.1.2) for $|\Delta p_2'|$ due to the ingestion and evacuation of a swirl change has good predictive value (within 20%). For $(\dot{m}_{\theta,1}/(\dot{m}_{\text{ax}}+\dot{m}_{\theta,\text{st,r}}))^2 > 0.08$ only one point was evaluated using the QSM, based on the steady flow data displayed in Fig. 5 (triangles). The QSM predicts the amplitude due to evacuation and the complete ingestion (first plus second stage) response, within a factor of two. Whereas it overestimates the first stage ingestion amplitude by ca. 50%. Thus, the data presented in this section point to a QSM having at the very least an order-of-magnitude prediction ability.

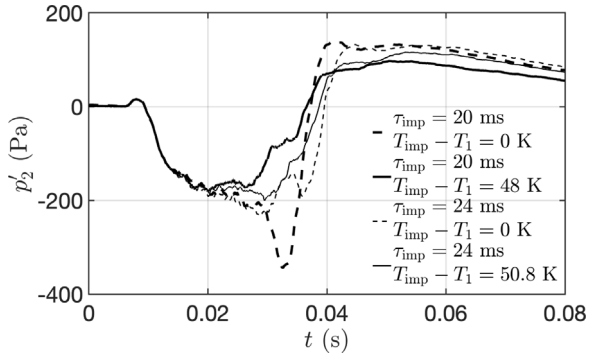

Fig. 16. Comparison of the downstream acoustic response p_2' to tangential-injection for $p_{\mathrm{imp}} = 6.2$ bar, $\tau_{\mathrm{imp}} = 20$ ms (thick lines) and $\tau_{\mathrm{imp}} = 24$ ms (thin lines). The dashed and the solid lines correspond to unheated- and heated-air tangential-injection experiments, respectively.

3.5.1. Order-of-magnitude estimate of mass-flow modulation

Eq. (A.5) in combination with the steady-state measurements of $p_{1,\mathrm{st}}/p_{\mathrm{th}}$ (Fig. 6), allows one to estimate $u_{\theta,\mathrm{th}}$. Using $u_{\theta,\mathrm{th}}$ as an input in [16]

$$\frac{\Delta\dot{m}}{\dot{m}^*} = \left(1 - \frac{(\gamma-1)}{(\gamma+1)}\left(\frac{u_{\theta,\mathrm{th}}}{c^*}\right)^2\right)^{\frac{\gamma+1}{2(\gamma-1)}} - 1 \tag{10}$$

where

$$c^* = \frac{c_1}{\sqrt{\frac{\gamma+1}{2}}} \tag{11}$$

allows one the estimate the relative mass-flow modulation $\Delta\dot{m}/\dot{m}^*$.

For the highest steady tangential mass-flow rates considered in the experiments, one has $p_{1,\mathrm{st}}/p_{\mathrm{th}} \simeq 2.233$ (see Fig. 6). Using the above described approach, one finds $\Delta\dot{m}/\dot{m}^* \simeq 0.2$.

The amplitude $\Delta p_2' \simeq 1.1$ kPa observed for the perturbation of highest-intensity steady background swirl in Fig. 14 corresponds to a change in mass flow $\Delta\dot{m}/\dot{m} \simeq \Delta p_2'/(\rho_2 c_2 U_2) = 0.4$. This is double theoretically predicted value using $p_{1,\mathrm{st}}/p_{\mathrm{th}}$. Thus, the order-of-magnitude of the mass-flow modulation observed here is such that a linearized theory (e.g. Howe and Liu's [25]) is not adequate.

Note that, as shown in Fig. 15, the prediction of the acoustic signal $\Delta p_2'$ based on the empirical quasi-steady model is half of the observed signal. Furthermore, the quasi-cylindrical model with uniform azimuthal velocity implies a uniform pressure at any cross-section. At the center of the actual flow there is a reduction of pressure of the order of $\rho_{\mathrm{th}} u_{\theta,\mathrm{th}}^2 \sim 0.25$ bar due to the centrifugal force in the swirl for $p_{\mathrm{th}} = 0.68$ bar. A numerical study is necessary to obtain a better prediction taking the non-uniformity of the flow into account, but at least the simple quasi-steady theory does provide an order of magnitude prediction.

4. Entropy–swirl–nozzle interaction experiments: results and analysis

4.1. Influence of injection-air temperature on downstream signal

In Fig. 16, low-pass filtered signals (and phase averaged over 10 consecutive experiments) due to the tangential injection of unheated and heated air are compared, for $\dot{m}_{\mathrm{ax}} = 1.194 \times 10^{-2}$ kg s^{-1}. The signals indicated with thick lines were obtained with $\tau_{\mathrm{imp}} = 20$ ms, and those indicated with thin lines with $\tau_{\mathrm{imp}} = 24$ ms. For both τ_{imp}, a short positive pulse is observed ($t = 8$ ms) at the start of impulsive injection. This is commonly referred to as direct sound [11,13,21]. After this pulse the acoustic signal due to unsteady swirl–nozzle interaction follows.

In both the unheated- and heated-air injection cases, one observes a strong negative swirl-ingestion pressure signal of amplitude $p_2' \simeq -190$ Pa. Around $t = 20$ ms, approximately 12 ms after the swirl ingestion pulse, one observes a difference, $\Delta p_2'$, in p_2' between the heated- and unheated-air tangential injection. This delay in arrival of heated air at the nozzle, indicates that the swirling fluid ingested by the nozzle during the first 12 ms is not the tangentially-injected fluid. This indicates that – before it reaches the nozzle – the tangential injection drives a rotation of the originally swirl-free fluid between the injection point and the nozzle inlet. In the $\Delta x_{\mathrm{inj}} = 85$ mm configuration, this effect is also expected to be responsible for the short 4 ms delay between: the acoustic pulse due to the onset of tangential injection and the start of indirect-noise due to swirl ingestion. This delay is significantly shorter than the convection time $\Delta x_{\mathrm{inj}}/U_1 = 7$ ms. As explained earlier for the larger injection distance $\Delta x_{\mathrm{inj}} = 185$ mm the delay does almost correspond to the convective delay time.

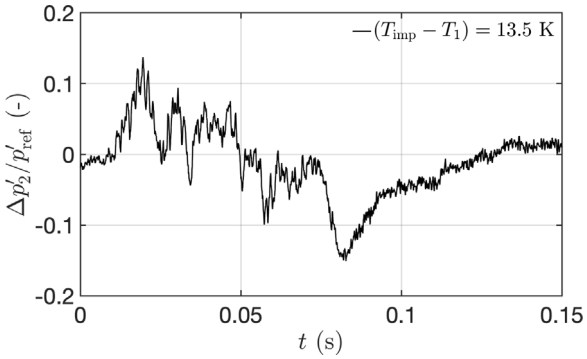

Fig. 17. Dimensionless difference $\Delta p_2'/p_{ref}'$ between heated and unheated impulsive-injection signals due to radial injection for $T_{imp} - T_1 = 13.5$ K, $p_{imp} = 5.2$ bar and $\tau_{imp} \simeq 62$ ms.

4.2. Quasi-steady model for the prediction of the response to an entropy patch

In the following, a theoretical reference amplitude p_{ref}' will be derived. p_{ref}' will be used to present the difference between the signals due to heated- and unheated-air injection in a dimensionless form. Given that p_2' remains unaffected by upstream-traveling acoustic reflections for 140 ms; all experiments were carried out with $\tau_{imp} \ll 140$ ms. Thus, for modeling purposes the downstream acoustic pipe is treated as anechoic.

With that in mind, p_2' is taken to be related to the axial acoustic velocity fluctuation, u_2', in the downstream pipe, as follows:

$$p_2' = \rho_2 c_2 u_2' \tag{12}$$

Assuming a quasi-one-dimensional flow and quasi-steady behavior of the nozzle, and neglecting the effect of the downstream weak shock, the local Mach number $M \equiv u/c$ (where u is the axial-flow velocity and c the local sound speed) is only determined by the nozzle geometry. In this case, taking air to be an ideal gas, one has

$$\frac{u'}{U} = \frac{c'}{c} = \frac{T'}{2T} \tag{13}$$

where T is the local temperature. N.b., this is relation is equivalent to Equation (16) in Marble and Candel [17]. Using Eq. (13), one can find the theoretical downstream pressure amplitude induced by an abrupt change in upstream temperature ΔT_1 :

$$p_{ref}' = \rho_2 c_2 U_2 \frac{\Delta T_1}{2T_1} \tag{14}$$

where ρ_2 is the mean downstream density, c_2 is the downstream sound speed, $U_2 = 7.8$ m s^{-1} is the unperturbed main flow velocity downstream of the nozzle. Note that as $(U_1/c_1)^2 \ll 1$ and $(U_2/c_2)^2 \ll 1$: $\Delta T_1 \simeq \Delta T_2$.

Eq. (14), can be validated by using it to predict the maximum entropy-noise amplitude for a swirl-free case considered by Leyko et al. [19]. Indeed, for $\Delta T_1/T_1 = 9/300$ and an anechoic downstream-pipe termination, Leyko et al. [19] report a maximum amplitude of 47 Pa (Run 2D-1 case Figure 13(a)) using an analytical model and numerical flow simulations. Now taking $U_2 = 7.8$ m s^{-1}, $\rho_2 = 1.2$ kg m^{-3} and $c_2 = 343$ m s^{-1} substitution in Eq. (14), yields $p_{ref}' \simeq 48$ Pa. This confirms the validity of Eq. (14).

Assuming perfect mixing of the axial main flow with the either radially or tangentially injected air, one can estimate the change in upstream stagnation temperature, ΔT_{mix}, as:

$$\Delta T_{mix} = \frac{\dot{m}_{imp}}{\dot{m}_{imp} + \dot{m}^*}(T_{imp} - T_1) \tag{15}$$

For the case of heated injection, the reference amplitude p_{ref}' is then calculated by substituting ΔT_{mix} for ΔT_1 in Eq. (14).

4.3. Radial injection of heated air

In Fig. 17, for radial injection the dimensionless downstream acoustic signal difference $\Delta p_2'/p_{ref}'$, obtained with $p_{imp} = 5.16$ bar and $\tau_{imp} = 62$ ms is shown as a function of time t. $\Delta p_2'$, in Fig. 17, is the difference between p_2' recorded as a result of radial injection of heated air ($T_{imp} - T_1 = 13.5$ K) and unheated air ($T_{imp} - T_1 = 0$ K). After a 20 ms delay, one observes a fairly-weak oscillating signal with a dimensionless amplitude of ca. $|\Delta p_2'/p_{ref}'| \simeq 0.1$. The interpretation of the signal is made difficult by the limited low-frequency response of the microphone. That said, globally one observes an increase $\Delta p_2'/p_{ref}' \simeq 0.1$ when the heated air enters the nozzle and the opposite effect when it leaves the nozzle. The signal after $t = 70$ ms is mainly due to the step response of the microphone. The weakness of the amplitude $|\Delta p_2'/p_{ref}'|$ is speculated to be due to the diversion of heated air in the upstream direction towards the settling chamber. In other words, after radial injection only part of the heated air is thought to be ingested by the choked nozzle.

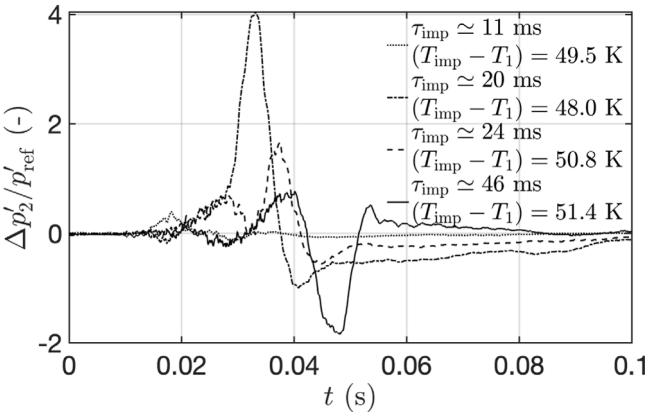

Fig. 18. Dimensionless difference $\Delta p'_2/p'_{ref}$ between heated and unheated impulsive-injection signals due to tangential injection. Doted line τ_{imp} = 12 ms, doted-dashed line τ_{imp} = 20 ms, dashed τ_{imp} = 24 ms, solid line τ_{imp} = 46 ms.

The authors hypothesize that radial injection strongly enhances turbulent mixing. In which case, the heated air is mixed with a much larger amount of unheated air than assumed when using Eq. (15). Furthermore, there is an important difference in the experimental setups for radial and tangential injection of heated air. Indeed, the hose segment between the heated reservoir and the fast injection valve is much longer for the radial injection than for the tangential injection; viz, 150 mm and 15 mm, respectively. The heat transfer to the hose is – as such – more important for radial injection experiments. Ergo, the temperature measurement in these experiments is less reliable.

4.4. Tangential injection of heated air

One notes that the axial mass-flow rate through the nozzle does not change as long as p_1 has not increased. In these experiments a significant increase in p_1 does not occur during the short-injection time $\tau_{imp} \leq 64$ ms.

The results shown in Fig. 18, obtained with tangential injection using $p_{imp} = 6.2$ bar, $T_{imp} - T_1 \simeq 50$ K and varied τ_{imp} contrast strongly with those for radial injection. Indeed, the amplitude $|\Delta p'_2/p'_{ref}| \simeq 4$ is significantly higher than for the radial-injection case. One notes that for the tangential-injection, $\Delta T_{mix} \simeq 0.24(T_{imp} - T_1) \simeq 13$ K. Ergo, the observed amplitude corresponds to a patch of air at temperature T_{imp} passing through the nozzle.

It is hypothesized that the impulsively-injected air initially accumulates upstream from the nozzle, because the axial mass-flow rate through the nozzle does not change instantaneously. After some time, the axial mass-flow rate through the nozzle decreases as a result of swirl ingestion [13].

The authors believe that the presently-reported data show that after tangential injection is halted, the accumulated higher-enthalpy gas (heated air patch) abruptly passes through nozzle. The result for τ_{imp} = 20 ms shows a strong positive acoustic peak of amplitude $\Delta p'_2/p'_{ref} \simeq 4$ around t = 35 ms. Note that the magnitude of this peak in the dimensionless signal is about four times larger than the reference amplitude p'_{ref} (Eq. (14)). This indicates that the accumulated heated air has a temperature closer to the injection reservoir temperature T_{imp} than to the perfect mixing temperature T_{mix} (Eq. (15)). Apparently in this particular experiment, the tangentially-injected heated air does not mix with the surrounding air.

This result confirms that deflection of tangentially-injected air in the upstream direction. Moreover, it points to the hypothesis of its accumulation – with limited mixing with the main flow – to be plausible. We note, that it is very similar to the hypothesis made to explain the second swirl-ingestion pulse in tangential-injection experiments with strong steady background swirl.

One also observes negative values of $\Delta p'_2/p'_{ref}$. At this point this intricate behavior is not readily understood. The role of the tangentially-injected flow's density on its mixing with the main flow could be investigated by comparison of experiments using injection gasses of different molecular weights (such as Argon, Neon and Helium). This would avoid complications due to heat transfer in the injection system. Moreover, to allow hundred consecutive repetitions of the injection experiment, it is easier to supply the injection reservoir by means of a high pressure bottle of a different gas than to – accurately and safely – heat up the corresponding air supply system. We note, that this repetition increases the signal to noise ratio. Furthermore, given that detailed non-intrusive measurements are troublesome, complementary numerical simulations which could provide quantitative analysis of this effect are recommended.

5. Conclusions

Original cold-gas unsteady swirl–choked–nozzle interaction experiments, with and without the presence of a steady-background swirl, have been presented. When no background swirl is present, the amplitude $|\Delta p'_2|_{BSF}$ of the downstream measured acoustic response was confirmed to scale with the square of the upstream injected tangential mass-flow rate $\dot{m}_{\theta,1}$; i.e., $|\Delta p'_2|_{BSF} \propto \dot{m}^2_{\theta,1}$.

Additionally, ϕ_θ the angle of upstream tangential injection ϕ_θ (defined relative to the direction normal to axial flow and tilted in the downstream direction) was changed from zero to 10° and found not to have a large influence on $|\Delta p_2'|_{\mathrm{BSF}}$. A quasi-steady model, based on steady-state measurements, was found to have good predictive value (within 50%) for $|\Delta p_2'|_{\mathrm{BSF}}$ due to swirl evacuation. Moreover, a systematic difference in $|\Delta p_2'|_{\mathrm{BSF}}$ due to ingestion and evacuation was observed. Initially a significant part of the tangentially-injected flow is deflected towards the upstream reservoir, because the nozzle cannot accommodate the increased mass flow. The rotating fluid initially entering the nozzle in the swirl-ingestion phase – as confirmed by experiments with injection of heated air – is rotation free fluid set into rotation by the injection.

The perturbation of a low-intensity steady background swirl was found to produce a downstream acoustic response very similar to the background-swirl free case. This was not true for the perturbation of a high-intensity background swirl. In this case, for short injection-valve trigger times compared to the convection time along the upstream pipe segment ($\tau_{\mathrm{valve}} = 10$ ms): $|\Delta p_2'|/|\Delta p_2'|_{\mathrm{BSF}} \simeq ((\dot{m}_{\theta,\mathrm{l}} + \dot{m}_{\theta,\mathrm{st,r}})^2 - \dot{m}^2_{\theta,\mathrm{st,r}})/(3\dot{m}^2_{\theta,\mathrm{l}})$ where $|\Delta p_2'|$ and $|\Delta p_2'|_{\mathrm{BSF}}$ are the amplitudes in the presence and absence of a background swirl. For long-injection valve trigger times ($\tau_{\mathrm{valve}} = 70$ ms) the negative mass-flow rate modulation occurred in two stages. In the first stage, a negative acoustic response occurs due to swirl-change ingestion, in a manner very much like the background-swirl free case. In the second stage, a much stronger negative acoustic response occurs after a time delay of ca. 40 ms. It is hypothesized that the second stage is due to the release of accumulated swirl upstream of the injection point by a sudden flow instability. This second stage is followed by a positive acoustic response due to an increase axial mass-flow rate, which is attributed to evacuation of the swirl perturbation by the nozzle. The amplitudes of the observed acoustic responses were found to scale with the square of the unsteady part of the tangential injection mass-flow rate; i.e., $|\Delta p_2'| \propto (\dot{m}_{\theta,\mathrm{l}} + \dot{m}_{\theta,\mathrm{st,r}})^2 - \dot{m}^2_{\theta,\mathrm{st,r}}$. A quasi-steady model for high-intensity background swirl cases, based on steady-state measurements, is proposed and found to predict $\Delta p_2'$ within a factor 2.

Preliminary results show that there is an influence of swirl on entropy-patch choked-nozzle interaction sound. In the cases where heated air was injected tangentially, the data shows signs of accumulation of heated air without mixing upstream from the choked nozzle. This pocket of heated air induces a strong positive pressure pulse $\Delta p_2'$ as it is ingested by the convergent–divergent nozzle after the injection is stopped. This is followed by a reduction of $\Delta p_2'$ compared to the unheated-air injection. Heat transfer between the heated air and the walls is a problem in such experiments. Ergo, we suggest that – instead of using heated air – this phenomenon be further studied by injection in the main air flow of gases of different molecular weights than the gas in the main flow, such as Argon, Neon or Helium.

Both the experiments with unsteady tangential injection in the presence of a strong permanent swirl and the tangential injection of heated air, indicate complex transient behavior, which will limit the possibility of a rapid pneumatic control of flow conditions through the nozzle.

Acknowledgments

Lionel Hirschberg carried out the reported measurements while he was the beneficiary of a Deutsches Zentrum für Luft- und Raumfahrt (DLR) - Deutscher Akademischer Austauschdienst (DAAD) postdoctoral fellowship (no. 57424730). The authors thank Angelo Rudolphi, Sebastian Kruck, Oliver Klose, Nico Seiffert and Lech Modrzejewski for the technical support. Analysis and redaction of this text were performed while Lionel Hirschberg was a member of Aimee Morgans' group at Imperial College London — the authors thank Aimee Morgans for her support. Lionel Hirschberg thanks Catherine Lemaitre and Assa Ashuach for their help.

Appendix A. Estimation of the azimuthal velocity from pressure measurements at the nozzle throat

Assuming a steady isentropic frictionless flow from the nozzle inlet to the throat of the nozzle one finds a relationship between the measured ratio $p_{1,\mathrm{st}}/p_{\mathrm{th}}$ and the Mach number M_{th} at the wall in the throat:

$$\frac{T_1}{T_{\mathrm{th}}} = \frac{c_1^2}{c_{\mathrm{th}}^2} = 1 + \frac{\gamma - 1}{2} M_{\mathrm{th}}^2 = \left(\frac{p_{1,\mathrm{st}}}{p_{\mathrm{th}}}\right)^{\frac{\gamma-1}{\gamma}} \tag{A.1}$$

or

$$M_{\mathrm{th}} = \sqrt{\frac{2}{\gamma - 1}\left(\left(\frac{p_{1,\mathrm{st}}}{p_{\mathrm{th}}}\right)^{\frac{\gamma-1}{\gamma}} - 1\right)} \tag{A.2}$$

For an axial symmetric flow, one has

$$\frac{u_{\theta,\mathrm{th}}}{c_{\mathrm{th}}} = \sqrt{M_{\mathrm{th}}^2 - \left(\frac{u_{x,\mathrm{th}}}{c_{\mathrm{th}}}\right)^2} \tag{A.3}$$

For a quasi-cylindrical uniform flow, the following choking condition holds [16]

$$\frac{u_{x,\mathrm{th}}}{c_{\mathrm{th}}} = 1 \tag{A.4}$$

Substitution in Eq. (A.3), and using Eqs. (A.1) and (A.2), yields

$$u_{\theta,\mathrm{th}} = c_1 \left(\frac{p_{\mathrm{th}}}{p_{1,\mathrm{st}}}\right)^{\frac{\gamma-1}{2\gamma}} \sqrt{\frac{2}{\gamma-1}\left(\left(\frac{p_{1,\mathrm{st}}}{p_{\mathrm{th}}}\right)^{\frac{\gamma-1}{\gamma}} - 1\right) - 1} \tag{A.5}$$

Eq. (A.5) can be used to estimate $u_{\theta,\mathrm{th}}$. Once $u_{\theta,\mathrm{th}}$ has been calculated, the azimuthal velocity at the nozzle inlet, $u_{\theta,\mathrm{in}}$, is found using the conservation of angular moment, to wit:

$$u_{\theta,\mathrm{in}} = u_{\theta,\mathrm{th}} \frac{R_{\mathrm{th}}}{R_1} \tag{A.6}$$

This makes a rough estimation of the azimuthal velocity $u_{\theta,\mathrm{in}}$ close to the wall at the inlet of the nozzle possible. Clearly, the flow is not a uniform quasi-cylindrical flow. Therefore, more effort would be needed to obtain a more accurate estimation of this azimuthal velocity.

Appendix B. Reflection coefficient for acoustic waves at the nozzle inlet

Assuming a quasi-steady response of the nozzle, let us now calculate the reflection coefficient r_{nozzle} of acoustic waves at the nozzle inlet. Given, that the nozzle is choked: the nozzle inlet Mach number upstream from the nozzle is – for a frictionless steady flow – determined by the geometry of the nozzle. I.e., in first order approximation the ratio of nozzle inlet cross-sectional area to throat cross-sectional area. This implies that the relative changes in flow velocity u_1'/U_1 and sound speed c_1'/c_1 at the nozzle inlet must be equal, to wit

$$\frac{u_1'}{U_1} = \frac{c_1'}{c_1} \tag{B.1}$$

An incident acoustic wave p_1^+ and the reflected wave p_1^- will induce: a pressure fluctuation $p_1' = p_1^+ + p_1^-$ and an associated isentropic change in sound speed

$$\frac{c_1'}{c_1} = \frac{\gamma-1}{2\gamma}\frac{p_1'}{\gamma p_1}$$

where γ is the ratio of specific heats at constant pressure and volume, respectively. Furthermore, for an ideal gas, we have $\gamma p_1 = \rho_1 c_1^2$. The acoustic velocity perturbation is – for plane waves – given by $\rho_1 c_1 u_1' = p_1^+ - p_1^-$. After some algebra, one obtains:

$$r_{\mathrm{nozzle}} = \frac{p_1^+}{p_1^-} = \frac{c_1 - \frac{\gamma-1}{2}U_1}{c_1 + \frac{\gamma-1}{2}U_1} = 0.986 \tag{B.2}$$

Appendix C. Direct sound transmission

We consider a quasi-one dimensional steady flow through a choked nozzle with inlet cross-section A_1 and outlet cross-section A_2. Mass conservation implies:

$$A_1\rho_1 U_1 = \dot{m}_1 = \dot{m}_2 = A_2\rho_2 U_2 \tag{C.1}$$

where u_i $(i = 1, 2)$ is the axial flow velocity and ρ_i the density in section i. We note that the Mach number $M_i = u_i/c_i$, with c_i the sound speed, is small $M_i^2 \leq 10^{-3}$. Furthermore, as $M_1^2 \ll 1$ and $M_2^2 \ll 1$ and because of the total enthalpy conservation: $T_1 \simeq T_2$. Consequently one has $c_1 \simeq c_2$.

Moreover, when the throat of the nozzle with section A_{th} is choked, $A_{\mathrm{th}} = A^*$, the upstream Mach number M_1 is determined by the geometry of the nozzle. Because the geometry does not change — the Mach number M_1 remains constant. In particular, for a quasi-one dimensional frictionless steady flow of a perfect gas with heat capacity ratio γ, one has [32,33]:

$$\frac{A^*}{A_1} = M_1 \left(\frac{\frac{\gamma+1}{2}}{1+\frac{\gamma-1}{2}M_1^2}\right)^{\frac{\gamma+1}{2(\gamma-1)}} \tag{C.2}$$

Applying a small quasi-steady isentropic compression p_1' upstream from the nozzle, one has $u_1'/U_1 = c_1'/c_1$ (Eq. (B.1)), because M_1 remains constant. Using Eq. (B.1) and the isentropic relations for an ideal gas, and doing some algebra, yields

$$\frac{p_1'}{p_1} = \gamma\frac{\rho_1'}{\rho_1} = \frac{\gamma}{\gamma-1}\frac{T_1'}{T_1} = \frac{2\gamma}{\gamma-1}\frac{c_1'}{c_1} = \frac{2\gamma}{\gamma-1}\frac{u_1'}{U_1} \tag{C.3}$$

With this result and using the equation of continuity Eq. (C.1), one finds

$$\frac{(\rho_2 u_2)'}{\rho_2 U_2} = \frac{(\rho_1 u_1)'}{\rho_1 U_1} = \frac{\rho_1'}{\rho_1} + \frac{u_1'}{U_1} = \frac{\gamma+1}{2\gamma}\frac{p_1'}{p_1} \tag{C.4}$$

As $M_1^2 \ll 1$ and $M_2^2 \ll 1$ the pressures p_1 and p_2 are in good approximation equal to the total pressures (respectively upstream and downstream from the shock). Therefore, the specific entropy $s_2 - s_1$ generated by the shock is [32,34]:

$$\frac{s_2 - s_1}{R} \simeq \ln\left(\frac{p_1}{p_2}\right) \tag{C.5}$$

with $R = c_p - c_v$ the ideal gas constant.

Using $s_1' = 0$ one finds that the downstream entropy wave generated by the isentropic pressure fluctuation p_1' has an amplitude:

$$\frac{s_2'}{R} = \frac{p_1'}{p_1} - \frac{p_2'}{p_2} \tag{C.6}$$

Using the first law of thermodynamics, assuming a reversible process for an ideal gas

$$\mathrm{d}s = c_v \frac{\mathrm{d}T}{T} - R\frac{\mathrm{d}\rho}{\rho} = c_v\left(\frac{\mathrm{d}p}{p} - \frac{\mathrm{d}\rho}{\rho}\right) - (c_p - c_v)\frac{\mathrm{d}\rho}{\rho} \tag{C.7}$$

one finds:

$$\frac{s_2'}{R} = \frac{1}{\gamma - 1}\left(\frac{p_2'}{p_2} - \gamma\frac{\rho_2'}{\rho_2}\right) \tag{C.8}$$

Eliminating the entropy, one obtains from Eq. (C.6) and (C.8):

$$\frac{\rho_2'}{\rho_2} = \frac{p_2'}{p_2} - \frac{(\gamma - 1)}{\gamma}\frac{p_1'}{p_1} \tag{C.9}$$

Using the equation of continuity (Eq. (C.4)) and assuming an anechoic downstream pipe termination, one predicts (after some algebra) for the transmitted pressure fluctuation p_2':

$$p_2' = \rho_2 c_2 u_2' = \rho_2 c_2 U_2\left[\frac{(\rho_2 u_2)'}{\rho_2 U_2} - \frac{\rho_2'}{\rho_2}\right] = \frac{p_2}{p_1}\frac{M_2}{(1 + \gamma M_2)}\frac{(3\gamma - 1)}{2}p_1' \tag{C.10}$$

where the equation $\gamma p_2 = \rho_2 c_2^2$ was used.

For the example discussed in the main text ($p_\theta = 5$ bar, the amplitude of the initial downstream pressure wave p_1^+ induced by the opening of the valve has the amplitude $p_1^+ = 823$ Pa (see Fig. 8). The pressure fluctuation p_1' induced by reflection of this wave at the nozzle inlet has the amplitude $p_1' = p_1^+(1 + r_{nozzle}) = 1634$ Pa. Using Eq. (C.10) with $p_1/p_2 = 1.12$, $M_2 = 0.020$ and $\gamma = 1.40$, one finds a transmitted-wave amplitude $p_2' = 47$ Pa. This is in satisfactory agreement with the observed transmitted-wave amplitude $p_2' = 60$ Pa (see Fig. 7).

It is noteworthy that if the transmitted acoustic-wave amplitude is estimated using the acoustic-energy conservation law, one has

$$|p_2'|^2 = |p_1^+|^2\frac{(1 + M_1)^2}{(1 + M_2)^2}\left(1 - r_{\mathrm{nozzle}}^2\frac{(1 - M_1)^2}{(1 + M_1)^2}\right) \tag{C.11}$$

Using $M_1 = 0.0364$, $c_1 = c_2$, $M_2 = M_1(A_1/A_2)(p_1/p_2)$, $r_{\mathrm{nozzle}} = 0.986$ and $p_1^+ = 823$ Pa one finds $|p_2'| = 321$ Pa, which is not in satisfactory agreement with the measured 60 Pa. A significant amount of the acoustic energy is absorbed by the shock wave in the divergent part of the nozzle.

The proposed model is only valid for low frequency perturbations. The fair agreement between theory and experiment is therefore surprising. An extensive more general discussion of the influence of the shock in the divergent part of the nozzle on the wave transmission is provided by Duran and Moreau [35].

References

[1] W.C. Strahle, On combustion generated noise, J. Fluid Mech. 49 (2) (1971) 399–414, https://doi.org/10.1017/S0022112071002167.

[2] A.P. Dowling, Y. Mahmoudi, Combustion noise, Proc. Combust. Inst. 35 (1) (2015) 65–100, https://doi.org/10.1016/j.proci.2014.08.016.

[3] A.S. Morgans, I. Duran, Entropy noise: A review of theory, progress and challenges, Int. J. Spray Combust. Dyn. 8 (4) (2016) 285–298, https://doi.org/10.1177/1756827716651791.

[4] K.W. Dotson, S. Koshigoe, K.K. Pace, Vortex shedding in a large solid rocket motor without inhibitors at the segmented interfaces, J. Propuls. Power 13 (2) (1997) 197–206, https://doi.org/10.2514/2.5170.

[5] S.J. Hulshoff, A. Hirschberg, G.C.J. Hofmans, Sound production of vortex nozzle interactions, J. Fluid Mech. 439 (2001) 335–352, https://doi.org/10.1017/S0022112001004554.

[6] J. Anthoine, J.-M. Buchlin, A. Hirschberg, Effect of nozzle cavity on resonance in large SRM: Theoretical modeling, J. Propuls. Power 18 (2) (2002) 304–311, https://doi.org/10.2514/2.5935.

[7] L. Hirschberg, S.J. Hulshoff, J. Collinet, C. Schram, T. Schuller, Vortex nozzle interaction in solid rocket motors: A scaling law for upstream acoustic response, J. Acoust. Soc. 144 (1) (2018) EL46–EL51, https://doi.org/10.1121/1.5046441.

[8] L. Hirschberg, S.J. Hulshoff, J. Collinet, C. Schram, T. Schuller, Influence of nozzle cavity on indirect vortex- and entropy-sound production, AIAA J. 57 (7) (2019) 3100–3103, https://doi.org/10.2514/1.J058138.

[9] L. Hirschberg, S.J. Hulshoff, Lumped-element model for vortex-nozzle interaction in solid rocket motors, AIAA J. 58 (7) (2020) 3241–3244, https://doi.org/10.2514/1.J058673.

[10] F. Bake, C. Richter, B. Muhlbauer, N. Kings, I. Rohle, F. Thiele, B. Noll, The entropy-wave generator (EWG): A reference case on entropy noise, J. Sound Vib. (2009) 574–598, https://doi.org/10.1016/j.jsv.2009.05.018.

[11] N. Kings, F. Bake, Indirect combustion noise: noise generation by accelerated vorticity in a nozzle flow, Int. J. Spray Combust. Dyn. 2 (3) (2010) 253–266, https://doi.org/10.1260/1756-8277.2.3.253.
[12] N. Kings, Indirect combustion noise: Experimental investigation of the vortex sound generation in nozzle flows, (Ph.D. thesis), Technische Universität Berlin, 2015.
[13] L. Hirschberg, F. Bake, K. Knobloch, S.J. Hulshoff, Swirl-nozzle interaction experiments: Influence of injection-reservoir pressure and injection time, AIAA J. 59 (7) (2021) 2806–2810, https://doi.org/10.2514/1.J060291.
[14] F. De Domenico, E. Rolland, J. Rodrigues, L. Magri, S. Hochgreb, Compositional and entropy indirect noise generated in subsonic non-isentropic nozzles, J. Fluid Mech. 910 (2021) A5 1–31, https://doi.org/10.1017/jfm.2020.916.
[15] M. Wellemann, N. Noiray, Experiments on sound reflection and production by choked nozzle flows subject to acoustic and entropy waves, J. Sound Vib. 492 (2021) 115799, https://doi.org/10.1016/j.jsv.2020.115799.
[16] L. Hirschberg, F. Bake, K. Knobloch, A. Rudolphi, S. Kruck, O. Klose, S.J. Hulshoff, Swirl-nozzle interaction experiment: Quasi-steady model based analysis, Exp. Fluids 62 (175) (2021) 1–16, https://doi.org/10.1007/s00348-021-03271-y.
[17] F.E. Marble, S.M. Candel, Coustic disturbance from gas non-uniformities convected through a nozzle, J. Sound Vib. 55 (1977) 225–243, https://doi.org/10.1016/0022-460X(77)90596-X.
[18] J.E. Ffowcs Williams, M.S. Howe, The generation of sound by density inhomogeneities in low mach number nozzle flows, J. Fluid Mech. 70 (3) (1975) 605–622, https://doi.org/10.1017/S0022112075002224.
[19] M. Leyko, S. Moreau, F. Nicoud, T. Poinsot, Numerical and analytical modelling of entropy noise in a supersonic nozzle with a shock, J. Sound Vib. (ISSN: 0022-460X) 330 (16) (2011) 3944–3958, https://doi.org/10.1016/j.jsv.2011.01.025.
[20] L. Hirschberg, S.J. Hulshoff, F. Bake, Sound production due to Swirl-Nozzle interaction: Model-based analysis of experiments, AIAA Avi. 2020 Forum (2020) 1–23, https://doi.org/10.2514/6.2020-2532, Virtual Event, June 15-19.
[21] L. Hirschberg, S.J. Hulshoff, F. Bake, Sound production due to Swirl–Nozzle interaction: Model-based analysis of experiments, AIAA J. 59 (4) (2021) 1269–1276, https://doi.org/10.2514/1.J059669.
[22] L. Hirschberg, F. Bake, S.J. Hulshoff, Sound production due to main-flow oriented vorticity-nozzle interaction in absence of a net swirl, in: 28th AIAA/CEAS Aeroacoustics Conference, Southampton, UK, 2022.
[23] J.-Y. Lestrade, J. Anthoine, A. Musker, A. Lecossais, Experimental demonstration of an end-burning swirling flow hybrid rocket engine, Aerosp. Sci. Technol. (ISSN: 1270-9638) 92 (2019) 1–8, https://doi.org/10.1016/j.ast.2019.05.057.
[24] G. Sharma, J. Majdalani, Effects of nozzle inlet size and curvature on the flow development in a bidirectional vortex chamber, Phys. Fluids 33 (9) (2021) 093607, https://doi.org/10.1063/5.0066121.
[25] M. Howe, T. Liu, The generation of sound by vorticity waves in swirling duct flows, J. Fluid. Mech. 81 (1977) 369–383, https://doi.org/10.1017/S0022112077002109.
[26] A. Mager, Approximate solution of isentropic swirling flow through a nozzle, J. Am. Rocket Soc. 31 (1961) 1140–1148, https://doi.org/10.2514/8.5732.
[27] L.J. Batson, R.H. Sforzini, Swirling flow through a nozzle, J. Spacecr. Rockets 7 (2) (1970) 159–163, https://doi.org/10.2514/3.29892.
[28] P.W. Carpenter, A general one-dimensional theory of compressible inviscid swirling flows in nozzles, Aeronaut. Quart. 27 (1976) 201–216.
[29] J.C. Dutton, Correlation of nozzle performance degradation due to Swirl, J. Propuls. Power 5 (1) (1989) 126–128, https://doi.org/10.2514/3.23125.
[30] D. Neuhaus, I. Röhle, Schnellschaltende Ventile für Anwendungen in der Luft und Raumfahrt (Fast-switching valves for Aeropsace Applications), in: Deutscher Luft- Und Raumfahrtkongress (German Aerospace Conference), 2006.
[31] L. Hirschberg, F. Bake, K. Knobloch, S.J. Hulshoff, Main flow oriented vorticity noise experiments, in: INTER-NOISE 2022, Glasgow, UK, 2022.
[32] A. Shapiro, The Dynamics and Thermodynamics of Compressible Fluid Flow, Vol. I, The Ronald Press Company, NY, USA, 1953.
[33] P.A. Thompson, Compressible-Fluid Dynamics, MacGraw Hill, NY, USA, 1972.
[34] J. Owczarek, Fundamentals of Gas Dynamics, International Book Compagy, Scranton, Pennsylvanis, 1964.
[35] I. Duran, S. Moreau, Solution of the quasi-one-dimensional linearized Euler equations using flow invariants and the magnus expansion, J. Fluid Mech. 723 (2013) 190–231, https://doi.org/10.1017/jfm.2013.118.